Synthesis, Characterization, and Second Harmonic Generation of Multiferroic Iron-Doped Lithium Niobate Powders

Mónica J García-Rodríguez, Oswaldo Sánchez-Dena, Omar A Velasco-Cortez, César L Ordóñez-Romero, Milton O Vázquez-Lepe, Rurik Farías, Christian Jonin, Pierre-François Brevet, Jorge-Alejandro Reyes-Esqueda

Synthesis, Characterization, and Second Harmonic Generation of Multiferroic Iron—Doped Lithium Niobate Powders

Mónica J. García-Rodríguez,[1] Oswaldo Sánchez-Dena,[1,2]* Omar A. Velasco-Cortez,[3] César L. Ordóñez-Romero,[3] Milton O. Vázquez-Lepe,[4] Rurik Farías,[1] Christian Jonin,[5] Pierre-François Brevet,[5] and Jorge-Alejandro Reyes-Esqueda[3,6]

[1]*Instituto de Ingeniería y Tecnología, Universidad Autónoma de Ciudad Juárez, Av. Del Charro 450 Norte, Ciudad Juárez, Chihuahua, 32310, México*

[2] *CONAHCYT Consejo Nacional de Humanidades Ciencias y Tecnologías, Av. Insurgentes Sur 1582, Col. Crédito Constructor, Benito Juárez, Ciudad de México, 03930, México*

[3] *Instituto de Física, Universidad Nacional Autónoma de México, Circuito de la Investigación, Científica, Ciudad Universitaria, Coyoacán, Ciudad de México, 04510, México*

[4] *Departamento de Ingeniería de Proyectos, Universidad de Guadalajara, Guadalajara, 45100 Jalisco, México*

[5] *Institut Lumière Matière, Université Claude Bernard Lyon 1, UMR CNRS 5306, Campus LyonTech La Doua, Bâtiment Alfred Kastler, 10 Rue Ada Byron, Villeurbanne, 69622, France*

[6] *Département de Physique, Faculté des sciences, Université de Sherbrooke, Québec J1K 2R1, Canada*

Corresponding Author :
Oswaldo Sánchez-Dena, oswaldo.sanchez@conahcyt.mx, oswaldo.sanchez@uacj.mx

Keywords: Second Harmonic Generation, random media, lithium niobate, metal—doping, ferroelectricity, ferromagnetism

ABSTRACT

Random granular media may exhibit characteristics more often related to ordered media. In the present work, this feature is observed in the polarized Second Harmonic Generation (SHG) response from reduced iron-doped lithium niobate (LN:Fe) powders, an effect that is not expected due to multiple scattering. Besides, this subsisting order property of the powders can be further controlled using magnetic induction to tailor the SHG response. The samples where characterized employing X-Ray Diffraction (XRD) and confocal Raman Spectroscopy. Their SHG response both in the absence and the presence of an external static magnetic field was then studied as the fundamental beam focus was translated from air into the powder. The SHG intensity polarization state was then studied as a function of the linear polarization of the fundamental beam for different fundamental beam focus depths. These results demonstrate that the SHG properties from LN:Fe powders can be modified through post-thermal treatment in a reducing atmosphere in view of photonic applications.

INTRODUCTION

Lithium niobate (LN, chemical formula $LiNbO_3$) is a synthetic bi-metallic oxide that presents high chemical stability and high melting point. It is insoluble in water and other organic solvents. Intrinsically, LN adopts a crystalline ferroelectric phase for a wide range of temperatures, from room temperature (RT) to approximately 1200°C. Large electro- and acousto-optical coefficients are ascribed to this phase, lending to this material attractiveness for applications in the fields of actuators, sensors, or transducers, notably for medical ultrasound devices, thermal sensors, sonar systems or precise positioners among others.[1,2] Ferroelectric LN possesses a large nonlinear optical coefficients too. Efficient coherent Second Harmonic Generation (SHG) can be obtained from this material within a broad range of fundamental excitation wavelengths with the corresponding second-order susceptibility tensor possessing three non-zero and independent tensor elements, namely d_{33}, d_{31} and d_{22}.[3] Coherent SHG is lost in the case of polycrystals, i.e. thin films or powders for example, due to intrinsic material randomization which could be twofold: spatial randomization (single nanocrystals in larger grains can have any possible orientation with respect to each other) plus randomization of the refractive index (it can vary from nanocrystal to nanocrystal according to the flexibility that characterizes the crystal structure of LN in adopting a continuous chemical composition within the range of ratios Li:Nb from 50.0:50.0 to approximately 48.4:51.6, RT conditions).

Recent developments have put LN into the scene in the rapidly growing field of applications in photonics,[4] to the extent that the once coined term ‘the silicon of photonics’ (2009) reverberates nowadays. LN is highlighted as the potential cornerstone in photonics, just as silicon has been for electronics.[5,6] But none of such applications could be possibly envisioned for polycrystals as incoherent light is a serious hindrance regarding any thinkable optical application. However, profit can still be obtained by studying the optical SHG response from polycrystalline solid solutions of LN. The incoherent feature of the response signal can be overcome by the combination of a proper experimental apparatus and the use of ultrasensitive detection devices such as cooled photomultipliers and charge-coupled device cameras. Any surface or interface can be assessed in this way by analysis of the SHG response.[7,8]

In this work, LN powders are being tested as they exhibit important ferromagnetic properties at RT when suitably doped with Fe ions and post-thermally treated in a reducing

atmosphere.[12] The connection between RT ferromagnetism in Fe—doped LN (hereafter referred to as LN:Fe) powders can be formally described based on the framework of Diluted Magnetic Oxides.[13] Our group has recently reviewed the subject, and the earlier and current investigations regarding the manifestation of magnetic and ferromagnetic behavior in LN:Fe (single crystals and polycrystals) have been discussed in detail.[14] In the present research, the consequences of the ferromagnetism properties of the LN:Fe powders are investigated and the order/disorder of the powders discussed using the SHG process and the deviation from the expected response from purely random powders.[15, 16]

RESULTS AND DISCUSSION

A total of 21 samples were synthesized. They can be classified into three main groups after the application of post-thermal treatments: untreated, reduced and oxidized samples. According to this classification, the samples have been labeled as shown in Table 1.

Table 1. *Nomenclature of the synthesized samples.*

Fe—doping concentration → [wt. % Fe_2O_3]	0[a)]	0.8	1.5	2.2	3.3	4.5	6.0
Untreated	pLN	8LN:Fe	15LN:Fe	22LN:Fe	33LN:Fe	45LN:Fe	60LN:Fe
Reduced	pLN-re	8LN:Fe-re	15LN:Fe-re	22LN:Fe-re	33LN:Fe-re	45LN:Fe-re	60LN:Fe-re
Oxidized	pLN-ox	8LN:Fe-ox	15LN:Fe-ox	22LN:Fe-ox	33LN:Fe-ox	45LN:Fe-ox	60LN:Fe-ox

[a)] The pristine samples

Controlling the oxidization state of the samples is important because reduced LN:Fe powders have shown a saturation magnetization about two orders of magnitude higher than the corresponding oxidized samples.[12] The coexistence of valence states Fe^{2+} and Fe^{3+} in LN:Fe nanocrystalline powders has been reported where a ratio of 0.15 holds for untreated samples.[17] The value can be lowered by the application of a suitable oxidizing thermal treatment, or rather, a reducing atmosphere can be used to reach a stable thermodynamical state for which the fraction of the Fe^{2+} population is close to 1. Oxidized samples are regularly thought of as passivated samples in the sense that no oxygen vacancies (V_O) are expected in these samples. Thus, the redox state of the samples can be effectively controlled if the reducing treatments are applied first and oxidation takes place second. All the oxidized samples studied in the present contribution were first reduced. Reproducible and consistent

results are expected with this approach. On the other hand, because LN is tacitly acknowledged to be a unique oxide without V_O's,[18] no significant differences are expected between untreated LN:Fe and oxidized LN:Fe-ox powders, neither structurally nor regarding their performances for nonlinear optics. In order to observe the impact of the state of the LN:Fe powders, thorough characterization was performed.

2.1. Characterization

2.1.1. X-Ray Diffraction

Figure 1 displays the recorded XRD patterns of (a) the untreated pristine LN powders (sample pLN), (b) the raw iron oxide powder used for the Fe—doping and its evolution after being reduced and oxidized and (c) the reduced LN:Fe samples. In Figure 1(a), the Bragg reflections comprise only peaks of a trigonal crystal structure with a hexagonal basis (lattice constants a = b = 0.515 nm and c = 1.386 nm) indicating the formation of the stable crystal structure $LiNbO_3$ (COD 2101175). Original diffraction data come from the Crystallographic Open Database.[19] An averaged ratio Li:Nb = 48.9:51.1 is determined after structural refinement by the Rietveld method and the use of Eq.(2) in Ref. 20 within the given absolute accuracy.[20] The pristine samples are thus off-stoichiometric with a chemical composition close to the congruent point, namely Li:Nb = 48.5:51.5. The population of intrinsic point defects is therefore rather high as targeted because the doping process becomes synergetic when cationic vacancies are disposable. Figure 1(b) shows that Fe_2O_3 powder on the opposite when undergoing phase-transitions into metallic iron (α-Fe, JCPDS PDF 00-006-0696) recovers its structural characteristics (hematite- Fe_2O_3, JCPDS PDF 04-015-6943) after being subjected to the same thermal treatments as those used for the pLN and LN:Fe samples, i.e. reduction and oxidation. Original diffraction data where taken from the Powder Diffraction File (ICDD®).[21]

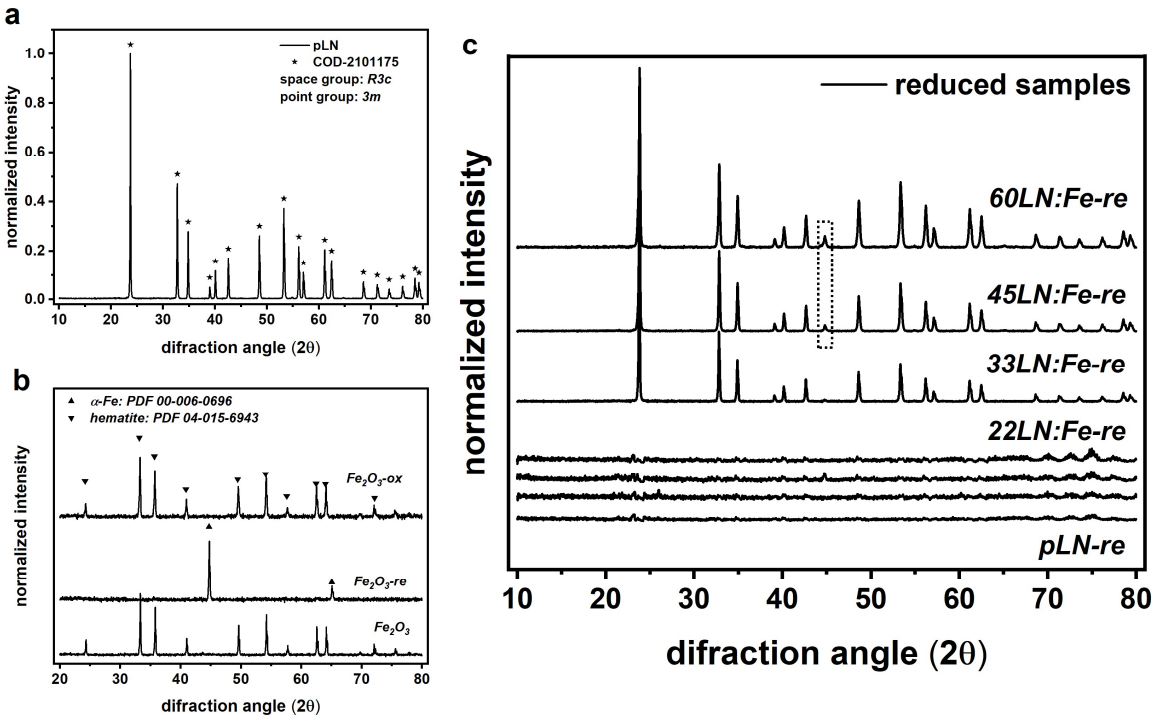

Figure 1 : *XRD characterization of the LN samples. (a) As obtained (without post-thermal treatment) pristine lithium niobate powders with near-congruent chemical composition denoted by a ratio Li:Nb = 48.91:51.1. (b) Iron oxide powders converted into powdered metallic iron and then recovered in their initial phase when first reduced and oxidized afterwards. (c) Reduced Fe—doped lithium niobate powders where the two samples of the highest doping concentration show the existence in small proportions of metallic iron as a secondary phase (2θ ≈ 45°). For a doping concentration of 3.3 wt. % Fe_2O_3, and below, solid solutions of lithium niobate were obtained as inferred from the straight lines resulting from a direct comparison between the corresponding patterns and that of the untreated pristine sample.*

In Figure 1(c), it is worth noticing that in the ~50-65° 2θ range, four peaks of intermediate intensity are located close to six ones of the LN phase which are of intermediate intensity too. These data show the unaltered recorded XRD patterns only for the three cases of higher doping concentrations. Identical curves of nearly constant intensity in the whole studied 2θ range are shown from sample 22LN:Fe-re down to sample pLN-re: these diffraction data are processed by simply calculating the quotient (normalized data in both inputs) between the corresponding sample and the pLN-re sample. The observed common baseline is interpreted

as the obtention of solid solutions of LN. Chemical solubility can be reached beyond a doping concentration of 3.3 wt. % Fe_2O_3. The XRD pattern of sample 33LN:Fe-re is also rather clean as well resembles that of the pure ferroelectric $LiNbO_3$ phase : neither the Bragg reflections of secondary phases related to iron can be tracked nor those of the precursors used for synthesis. On the other hand, an additional reflection of small intensity can be observed ca. $2\theta = 45°$ for samples 45LN:Fe-re and 60LN:Fe-re. It pertains to the main diffraction peak of metallic iron (α-Fe, JCPDS PDF 00-006-0696) and its intensity is accordingly incremental to doping concentration. Interestingly, no distinctive features pointing towards having reached the limit of solubility at a doping concentration of 4.5 wt. % Fe_2O_3 can be observed in the XRD patterns of the untreated and oxidized sets of samples, (data not shown). This is possible due to an overlapping of diffraction peaks taking place in the 2θ range ~ 50-65°. Hence, possible misconceptions could arise regarding the structural characteristics of LN:Fe powders if they are not subjected to a reducing post-thermal treatment. However, as it is shown in Table 2, such a nefarious fact can be overcome with structural refinement : phase quantification analysis leads to correct conclusions irrespective of the oxidation state.

Table 2 : *Phase percentages in the synthesized samples, as obtained by simultaneous insertion of cards containing the Wyckoff positions of the involved crystal structures.*

Sample → [a)]	45Ln:Fe	45Ln:Fe-re	45Ln:Fe-ox	60Ln:Fe	60Ln:Fe-re	60Ln:Fe-ox
% LiNbO3	99.6	99.0	99.2	98.0	96.9	97.2
% α-Fe	0	1.0	0	0	3.1	0
% Hematite-Fe_2O_3	0.4	0	0.8	2.0	0	2.8

[a)] The remaining samples are 100% $LiNbO_3$

From the data available in Table 2, it can be argued that a maximum of 1% (3%) of the secondary phase is present in the powders doped with a 4.5 (6.0) wt. % Fe_2O_3. Herein, it is worth mentioning that in view of the study of the Second Harmonic Generation (SHG) response, another classification of the synthesized materials holds in terms of the concentration of doped iron, as it can be the lowest, intermediate or the highest one. For practical purposes, the 1% of the second phase is considered marginal within the scope of this research and, thus, the samples 45LN:Fe have been denoted as the highest cases in the SHG analysis. Meanwhile, refinement of the crystal structures also sheds some light on the local environment to the unit cell, that is, a glance into the distribution of intrinsic and extrinsic point defect complexes.[2] The evolution of the structure in terms of a parameter of synthesis

is conventionally assessed through the extraction of the resulting lattice constants for a given number of experimental points. Usually, small differences in plots having a lattice parameter as the ordered axis are more discernible or significant when the whole set of parameters is circumscribed into the unit cell volume defined with the formula $\sqrt{3}a^2c/2$ for a hexagonal setting.[2,18] The unit cell volumes related to all the polycrystalline samples synthesized in this work are shown in Figure 2(a). Correspondingly, Figure 2(b) shows that the mean crystallite size is of the order of 60-100 nm whereas Figure 2(c) indicates that the executed routines converged giving satisfactory agreements between empirical and calculated patterns. Continuous relaxation of the crystal structure holds for the reduced samples as inferred from the observed monotonic increase of the unit cell volume with the doping concentration. A change of rate takes place at point 22LN:Fe-re. On the other hand, as expected, the untreated and oxidized crystal structures show identical local environments up to a critical point of 45LN:Fe(-ox): relaxation of the structures takes place first, then followed by a contracting mechanism as the doping concentration increases (inflection points can be noted in 1.5 and 2.2 wt. % Fe_2O_3 samples).

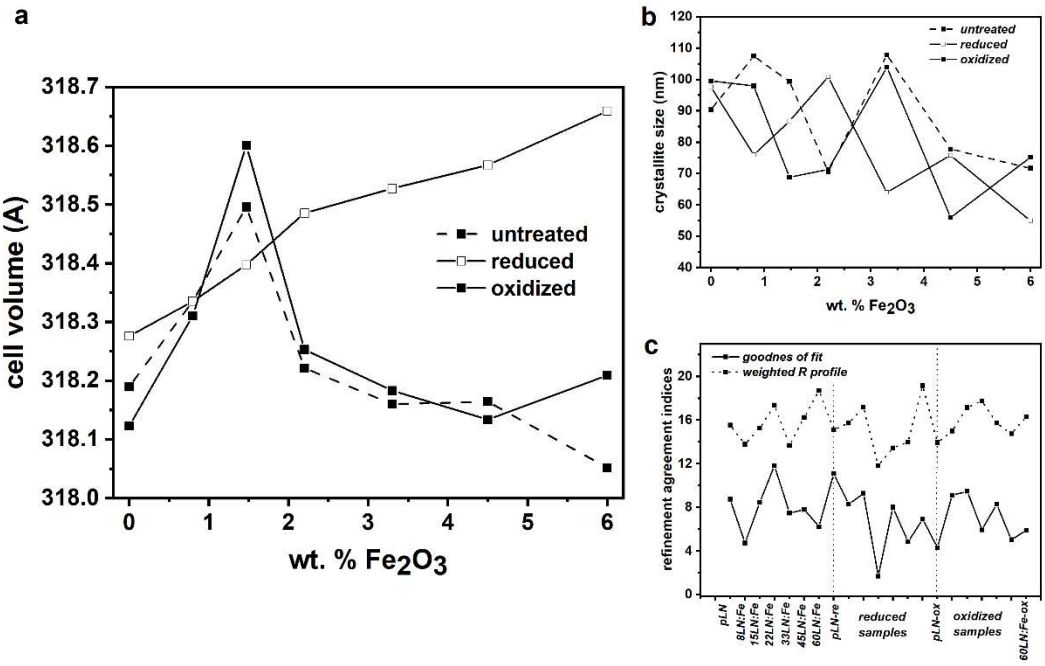

Figure 2 : *Crystal structure refinement with the Rietveld method. As a function of the doping concentration and of the applied post-thermal treatments : (a) Unit cell volumes in angstrom units. (b) Mean crystallite sizes calculated by implicit use of the Scherrer equation and weight*

averaging all the contributions to line broadening. (c) The estimated Rietveld error indices are less than or close to 10 %.

The most widely accepted defect scenario is the so-called lithium vacancy model.[14] Within this framework, neither oxygen vacancies (V_O) nor niobium vacancies (V_{Nb}) are assumed to exist, and the formation of a single Nb antisite defect (Nb_{Li}) is compensated by the formation of four Li vacancies (V_{Li}); its constitutional formula is $[Li_{1-5x}V_{4x}Nbx]NbO_3$, x=0.01.[22] Whilst it is here acknowledged that debate still prevails on the most appropriate defect model that solves electronic charge neutrality in off-stoichiometric LN –despite much research has been done on the subject—, it must also be stated that all the available evidence, collected either empirically or by ultimate computer simulations, points towards the univocal existence of Nb_{Li} antisites.[23] Such a point defect of intrinsic nature in LN denotes the occurrence of a stacking fault that compensates the charge unbalance, which is compromised by the inexorable tendency of this compound to crystallize forming solids with a Li deficiency (or Nb surplus).[2,14] Now in consideration of extrinsic defects in the fashion of elemental doping, conceiving that the inserted cations occupy first V_{Li}´s while substituting Nb in Li sites (replacement of Nb_{Li}´s) before it takes place a substitution mechanism for Li_{Li} and Nb_{Nb} entities, is nothing else but logic.

Many factors influence the observed trends in site occupancy and doping mechanisms (dopant concentration, ionic radii, valence states, etc.), but indeed, there seems to be concomitant evidence that all kind of dopants (irrespective of their nature or functionality when doped in LN) are predominantly localized in Li sites whenever small doping concentrations are used. Regarding the occupancy/substitution mechanisms in doped LN, two statements can be made. One is that the dopant ions tend to occupy Li sites first, either V_{Li} or Li_{Li}.[14] Second, if the content is being kept added, a critical instance is reached where the dopants begin to substitute Nb in Nb sites just before the chemical solubility of the pristine LN crystal structure is exhausted.[14] Naturally, the latter depends on the initial intrinsic defect structure, that is, the number of available V_{Li}´s and Nb_{Li}´s which is characterized by the macrostate chemical composition with a given ratio [Li]/[Nb] < 1. Such a devised picture is constructed upon several reports where Mg^{2+} and other optical damage-resistant ions (ODRI) have been used as doping entities. Recently, Kovacs et al. have observed the same trends for ODRI in some transition metals and in some lanthanide trivalent rare-earth ions too.[24] Regarding the cases of similar LN:Fe systems, there is evidence that iron tends to occupy Li sites rather than Nb

sites, irrespective of the oxidation state.[25] Some pioneering works focused on controlling the Fe^{2+} and Fe^{3+} populations employing annealing (of post-thermal treatments) are also worth mentioning.[26]

Although various counter examples can be found in the available literature,[14] it is thus possible to conceptualize that all kind of impurity ions adjust to the following order: 1) simultaneous occupation of lithium vacancies and substitution of Nb antisites, and (once depleted) 2) substitution for Li in Li sites followed by, 3) substitution for Nb in Nb sites, and 4) soon afterwards the limit of solubility is reached and segregation follows upon adding further doping content. If such a depiction is adopted, then it is convenient to define the critical instances of the starting points of stages 2) and 3) as the first concentration threshold (FCT) and the second concentration threshold (SCT), respectively. The significance of the term ′concentration threshold ′ herein stated has been proposed in earlier Refs. 18 and 24b and it also must be noted that it differs slightly from the sense that is usually attributed to it within the subfield of knowledge regarding LN doped (only) with ODRI.

Hence, in consideration of the discussion given in the preceding paragraphs, the trends shown in Figure 2(a) can be interpreted as follows. The FCT of the synthesized LN:Fe powders is reached between the doping concentrations of 1.5 and 2.2 wt. % Fe_2O_3. Post-thermal treatment in a reducing atmosphere is only sensitive to the chemical/physical instance where all the Li vacancies have been filled while all the Nb antisites are completely removed whereas the untreated and oxidized curves discriminate between both occupancy/substitution mechanisms. Under the assumption that most of the doped Fe ions share a common 3+ oxidation state for the untreated and oxidized samples, the observed increasing-decreasing-constant behavior in Figure 2(a) can be understood in simple terms of atomic size effects and their influence within the crystal structure (see Table in the Supporting Information file for the effective ionic radii for the species of interest with 6-fold coordination).[27] Relaxation of the crystal structure follows the filling of vacant Li sites (V_{Li}^{-}) with Fe^{3+} of comparable larger dimensions, about 64.5 pm, up to point 15LN:Fe(-ox). Then, it contracts due to cationic interchange with slightly larger Nb_{Li}^{4+} (size of about 69 pm), up to point 22LN:Fe(-ox) where a change of rate in the ongoing contracting mechanism results from tuning the interchange to Li_{Li}^{+} (size of about 74 pm). At some stage between points 33LN:Fe(-ox) and 45LN:Fe(-ox), the atomic size effects should turn minimal because of the inferred cationic interchange with the regular Nb sites (Nb_{Nb}^{5+}, size of about 64 pm), as it can be confirmed with the observed nearly constant

behavior. It is noticed that the quotient between the atomic radii for Nb^{5+} and Fe^{3+} is 0.99. Likewise, if a multitudinous change in the oxidation state $Fe^{2+} \rightarrow Fe^{3+}$ is assumed after the application of the reducing treatment, the same comparative analysis can lead to a satisfactory explanation of the observed trend of the reduced samples (line with empty squares). However, besides the fact that Fe^{3+} possess the largest ionic radius compared to the rest of the discussed cationic species, perhaps it also should be considered that the thorough relaxation of the structure is possibly assisted by volumetric electronic charge redistributions arising from the multitudinous creation of oxygen vacancies at the surfaces.

LN powders of overall stoichiometric composition were used as the pristine samples and also fit into the present discussion, see Ref. 12. On the other hand, the second concentration threshold (SCT), cannot be resolved explicitly by refinement of the XRD results, Figure 2(a), while it is expected to lie somewhere in between points 3.3 and 4.5 wt. % Fe_2O_3. It will be shown that analysis of the Raman spectra not only confirms the entailed arguments concerning the FCT, but also sensitivity to the SCT can be reached. Lastly, Figure 2(a) can also be considered as an excerpt of evidence neglecting the aesthetic idea that off-stoichiometric LN can be turned stoichiometric through suitable doping, that is, by an effective elimination of intrinsic defects by filling of the vacancy sites.[14,28] That could only be strictly correct if, for a given doping concentration, the unit cell volume would result to be smaller than that of the pristine sample (off-stoichiometric in this work), since undoped (and post-thermally untreated) LN shows a characteristic structural relaxation in going from the stoichiometric chemical position to any off-stoichiometric point, see Figure 3 in Ref. 20, for example.

2.1.2. X-Ray Photoelectron Spectroscopy

Further characterization of a small set of reduced and oxidized samples was done using X-Ray Photoelectron Spectroscopy (XPS) to demonstrate that the doped Fe ions have reached a population fraction close to 1 with oxidation states of 2+ and 3+, respectively. The selected samples for analysis were pLN-ox, pLN-re, 22LN:Fe-ox and 22LN:Fe-re. Figure 3 and Table 3 display the obtained photoelectron spectra and the binding energy values, respectively. The graphics show the O 1s core level spectrum which is typical for oxides. All the spectra showed a shift in binding energy, and after curve fitting, the observed peaks were c.a. 529.1 eV, associated with the regular lattice of lithium niobate. In the pristine reduced sample, the peaks around 530.1 eV and 528.1 eV are associated to distortion of the lattice, as discussed

previously in the results obtained by structure refinement. According to the process of synthesis, the first stage was the application of a reduction treatment then followed by the oxidation treatment. In the reduction treatment a loss of oxygen occurs, creating oxygen vacancies and a reduction of Nb^{5+} to $Nb4^{+}$. In contrast, oxygen is absorbed during the oxidation treatment. Such diffusion of oxygen causes the changes in binding energies observed in the XPS spectra. On the other hand, regarding the iron doped sample with reduction treatment, the 531.2 eV peak is assigned to the vacancy region.[29] The highest energy observed in the present study corresponds to sample 2LN:Fe-re, as it is shown in Table 3. Due to charge compensation, higher proportions of Fe^{2+} induce the formation of oxygen vacancies. [29,30]

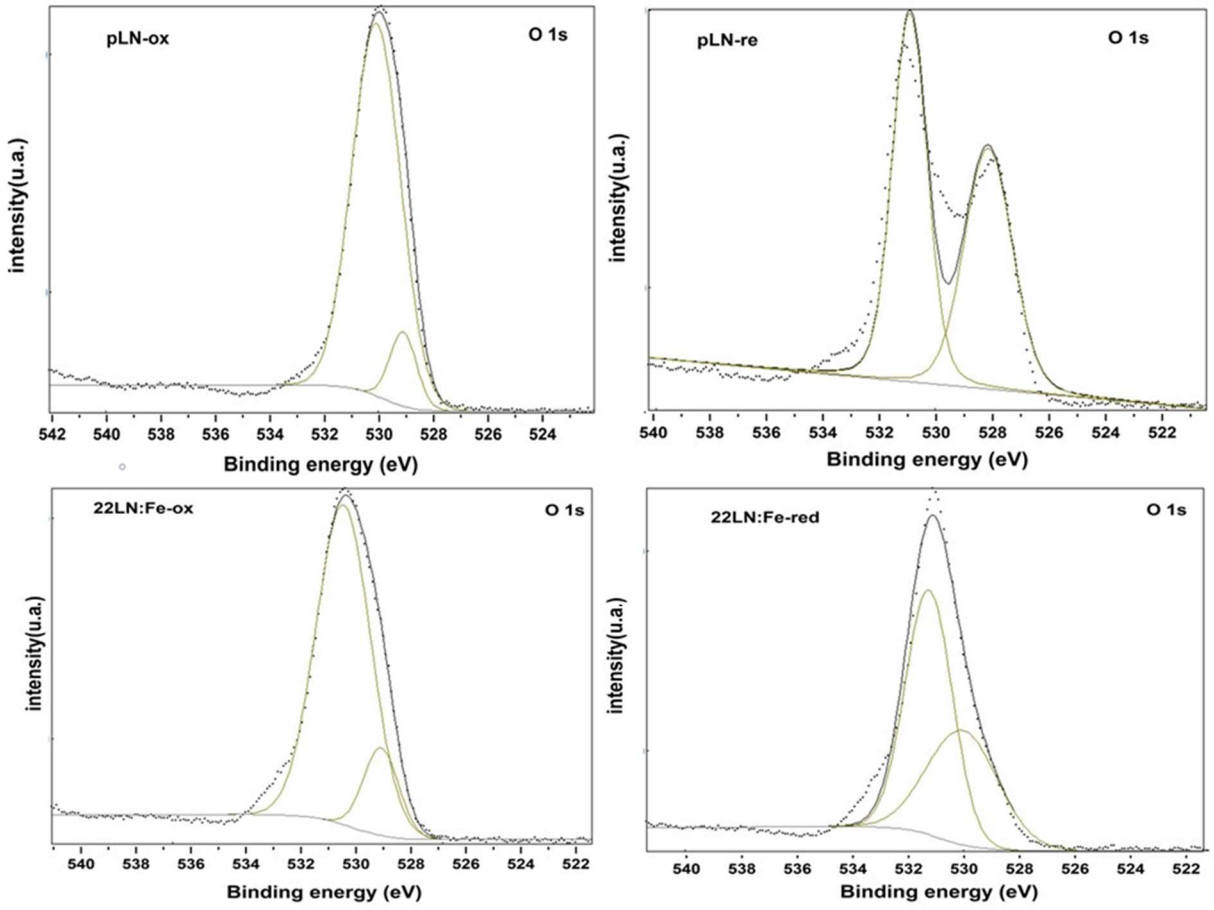

Figure 3 : *XPS spectra for O 1s in the LN samples with oxidation and reduction treatment.*

Table 3 : *Binding energy values obtained from peak fitting of XPS spectra.*

Sample	O 1s		Nb 3d		Fe 2p	
			$3d_{5/2}$	$3d_{3/2}$	$2p_{3/2}$	$2p_{1/2}$
pLN-ox	529.1 eV	530.1 eV	206.5	209.2	0	0
pLN-re	530.1 eV	528.1 eV	206.6	209.4	0	0
22LN:Fe-ox	530.3 eV	528.9	206.1	208.6	711.5	725.1
22LN:Fe-re	531.2 eV	530	206.8	209.5	711.3	724.2

In Figure 4, it is shown that the spin-orbit doublet corresponding to Nb 3d, contributions from $3d_{3/2}$ and Nd $3d_{5/2}$. In this case, the binding energies for most of the samples are around 206.1eV and 206.8 eV, which correspond to stable niobium Nb^{+5}. However, in the sample doped with an oxidation treatment, it can be noticed a reduction in the binding energy, particularly for the contribution $3d_{3/2}$ and it can be attributed for lithium substitution in regular sites. This causes a change in the density of charge for the Nb-Li bond, in correspondence with the discussion given from the XRD results, namely the observed reduction in the cell volume. On the other hand, the binding energies for contributions $3d_{5/2}$ and $3d_{3/2}$ increase in the case of sample 22LN:Fe-re, thus indicating the presence of oxygen vacancies produced during the reduction treatment and the presence of Fe^{2+} when lithium is replaced from its regular sites. The cell volume increases due to the larger ionic radii of Fe^{2+}, changing the charge density differently from the Fe^{3+} case.[31-33]

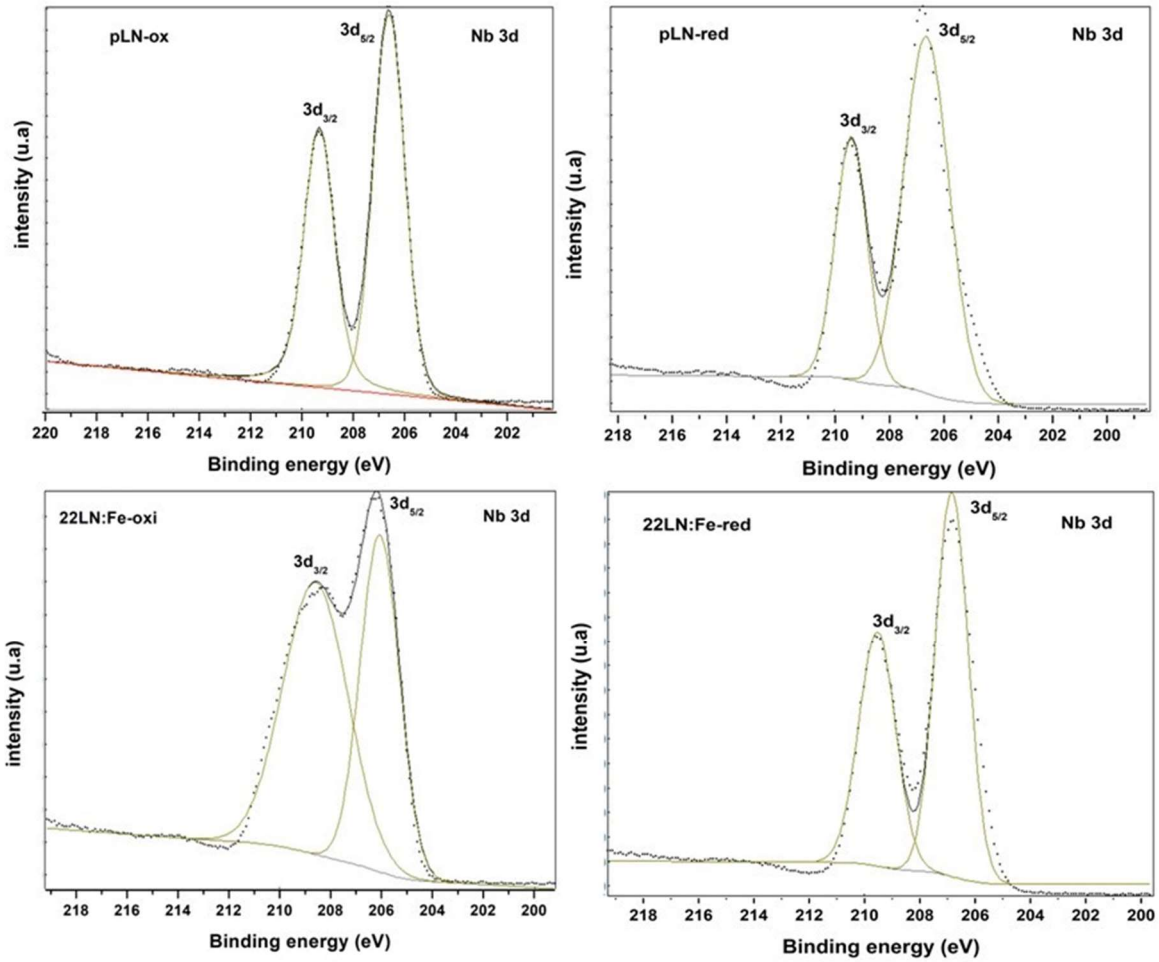

Figure 4 : *XPS spectra for Nb 3d in the LN samples with oxidation and reduction treatment.*

Lastly, Figure 5 shows the Fe 2p core level spectrum of samples 22LNFe-ox and 22LN: Fe-re. The two peaks correspond to Fe $2p_{3/2}$ and 2 $p_{1/2}$, and according to the obtained values, these samples have a mixture of both valences Fe^{+2} and Fe^{+3}. As it is shown in Table 3, the values of the peaks Fe $2p_{3/2}$ and Fe $2p_{1/2}$ are 711.5 eV and 725.1 eV for the oxidized sample, having a binding difference of 13.6 eV. These values are consistent with the trivalent oxidation state of iron. Likewise, for the reduced sample, the values of the peaks Fe $2p_{3/2}$ and Fe $2p_{1/2}$ are 711.3 eV and 724.2 eV, with binding energy difference of 12.9 eV. The decreasing in the binding energy is ascribed to the $Fe^{+3} \rightarrow Fe^{2+}$ reduction which comes from the increasing population of Fe^{2+}, as inferred from the $2p_{3/2}$ satellite observed in the spectrum at 715.7 eV. [34-36]

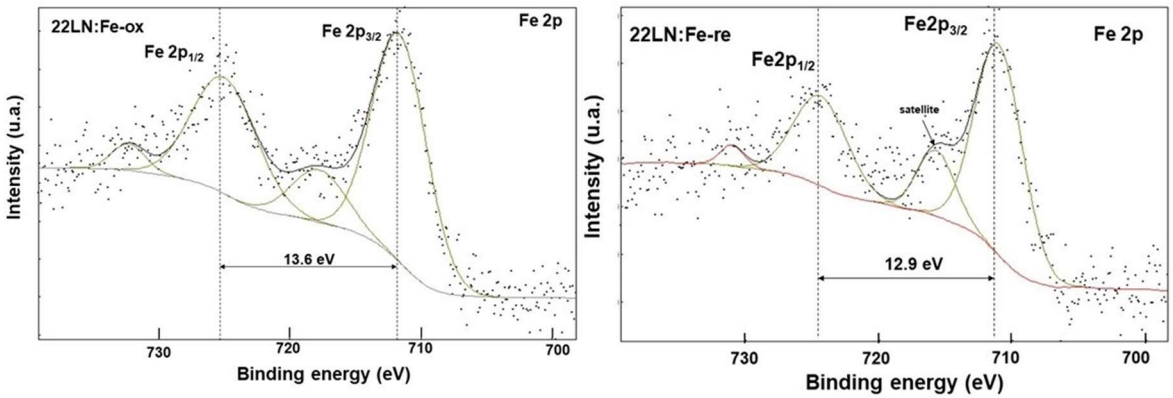

Figure 5 : *XPS spectra for Fe 2p in LN samples 22LN:Fe-ox and 22LN:Fe-ox.*

2.1.3. Confocal Raman Spectroscopy

The structural evolution of all samples was also investigated using Raman Spectroscopy. Representative data are shown in Figure 6. All spectra are plotted in the 100-1000 cm^{-1} relative wavenumber domain. Raman spectra resembling that of (pure ferroelectric) $LiNbO_3$ were recorded under the same experimental conditions for all the pristine and LN:Fe samples. Small deviations can be traced when the functional forms are compared to that corresponding to the Raman spectra of the untreated pristine sample, see Figure 6(a). They can be ascribed to slight registered differences regarding the centers and the linewidth of certain individual Raman bands or polar modes, from sample to sample. Such differences are likely to merge with the controlled defect structure or lattice re-ordering induced through elemental doping, i.e. the tuning of the phonon damping within the framework of damped harmonic oscillators. They hold for all instances, but they are more notorious for the reduced samples, Figure 6(b).

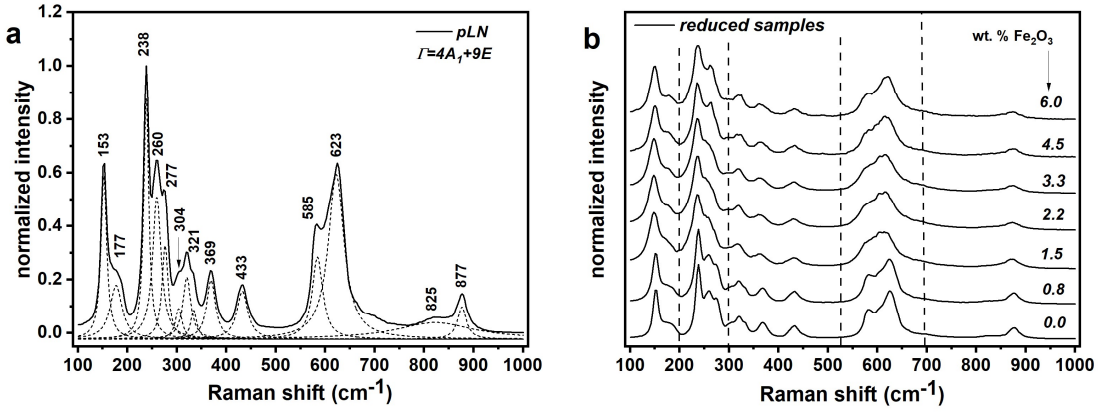

Figure 6 : *Raman spectra in the Stokes-frequency domain containing the fundamental lattice vibrations of lithium niobate (normalized to highest intensity). (a) Pristine powders, the dotted curves show the individual polar modes contributing to the full spectra. (b) The doping*

effect on the different modes of lattice vibration is more evident for the reduced LN:Fe powders, particularly near to $\Delta\tilde{\nu} = 250\ cm^{-1}$ *and* $\Delta\tilde{\nu} = 600\ cm^{-1}$.

In the framework of group theory, lattice vibrations pertaining to the LN system (space group R3c, point group 3m, RT) with vanishing k wave vector can be divided –in first approximation— into $5A_1$, $5A_2$, and 10 (twofold degenerate) E phonon branches.[37] Of these, one A_1 and E are the acoustic branches, the five A_2 fundamentals are Raman and infrared inactive, and the remaining 4 A_1 and 9 E optical branches are both Raman and infrared active.[38] Accordingly, with two molecules per unit cell, the irreducible representation of the optical modes can be expressed as $\Gamma = 4\ A_1 + 5A_2 + 9E$. Although the assignment of phonon modes in LN has been a subject of debate for a long time, the above description has only been adopted in few reports.[37,38] Because the A_2 are nonpolar and inactive, therefore there are 13 directional dispersion branches of phonons.

LN has a strong ionic role in what respects its overall chemical binding characteristics.[2] Hence, nominally the incident macroscopic electric field splits each A_1 and E modes into longitudinal optical (LO) and transverse optical (TO) components. Once the assignment of phonon modes has been done, the existent types of interactions between the structural units of LN can be deconvoluted into both components of each Raman active polar mode, as it has been described, for example, by Caciuc et al. (2000) and Fontana et al. (2015).[37] However, this type of analysis is only consistent with single crystals which have definite principal axes and, thus, knowledge of the state of linear polarization of the scattered light turns out to be of great importance. While the so-called selection rules for Raman active phonons can be determined univocally by standard methods of group theory, the relative intensities of given Raman modes can be rationalized according to the polarization directions of the incoming and scattered light.[38] In contrast, the distinction between the LO and TO components is not applicable for random media such as powders composed from myriads of single nanocrystals. The polarization information is lost because of the arbitrary orientations of each given crystallite, whereas the LO and TO can be assumed to overlap. For this reason, there is no need in using polarized Raman Spectroscopy to resolve all the 13 fundamental lattice vibrations of LN powders, see Figure 6(a) and the Experimental Section. Pezzotti (2013) has given an overall description of the LN main features of cation displacements in terms of relative wavenumber, summarized in a table presented in the Supporting Information file.

The small deviations shown in Figure 6(b) can be analyzed by rationalizing the characteristics of a given Raman band into the dimensionless parameter FWHM/$2x_c$ where the numerator stands for the Full Width at Half Maximum and the denominator for twice the spectral center of the Raman band. Both entries are influenced by the substitution mechanism that follows doping of the pristine LN structure with Fe ions and they are determined numerically after performing a multi-peak fitting of the Raman spectra using a Lorentzian line shape. Because the small deviations were also traced for the untreated and oxidized samples, although in minor proportions, this type of analysis was done for all samples. It was done once for each relative wavenumber domain of interest, namely the 200-300 cm^{-1} zone, the 550-700 cm^{-1} zone, the 100-200 cm^{-1} zone, and close to 877 cm^{-1}. In each case, the experimental data was abridged to specific limits sharing a common baseline (enlargement of the spectra around the zone of interest) and the number of peaks on the fitting varied from one to three depending on the case of analysis. The first two zones are those where the doping effect on the different modes of lattice vibration resulted to be more evident, as it is highlighted in Figure 6(b) with the dashed vertical lines. The remaining two zones were also studied so that the analysis could effectively cover the whole domain of fundamental Stokes modes, dividing it into the instances of low-, mid-, and high- Raman shift zones. They can also be considered as isolated contributions to the full Raman spectra when compared to the first two zones.

The results derived from the described analysis are shown in Figure 7. Initially, only the most intense Raman bands of each zone were targeted (solid curves in Figure 7(a) and Figure 7(b), but their respective adjoining polar modes have been also accounted for (dashed curves), to quantitatively assess any possible correlation between both contributions. Only the results for the most intense Raman bands of each zone (153, 623, and 877 cm^{-1}) are shown in Figure 7(c), where the untreated and oxidized samples have been represented with solid and dashed curves, respectively. It is also worth mentioning here that the trends resulting from using only the half-width (FWHM/2) are very similar to those shown in Figure 7, indicating that the latter can be interpreted based on the same mechanisms involved in the broadening of spectral bands, namely the increasing disorder in the lattice due to compositional inhomogeneity, crystal imperfections, and insertion of impurities and dopant ions, among others.

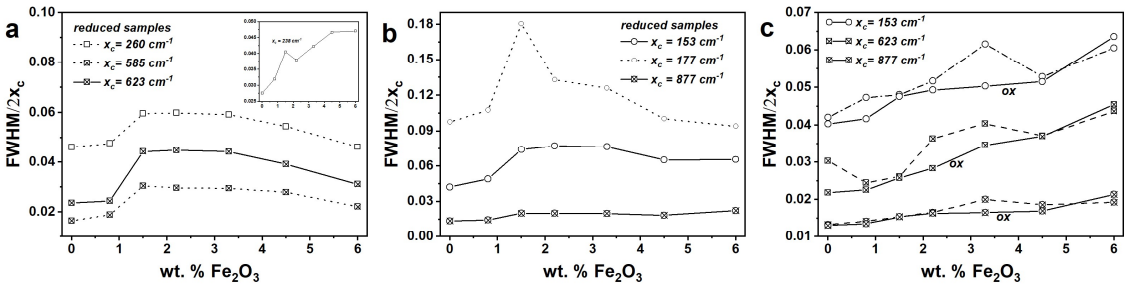

Figure 7 : *Half-width divided by the center of individual Raman bands of interest. In function of the doping concentration and of the applied post-thermal treatments: (a) Reduced samples ca. 238-260 cm^{-1} and 585-623 cm^{-1}, data for the 238 cm^{-1} band is shown in the inset figure. (b) Reduced samples ca. 153-177 cm^{-1} and 877 cm^{-1}. (c) Some results for the untreated and oxidized (solid curves) samples are given to show that no systematic behavior or characteristic trend can be ascribed to these cases.*

Interestingly, most curves shown in Figure 7(a) and Figure 7(b) show an identical behavior, excluding only the one obtained for the polar mode centered at x_c = 238 cm^{-1} (inset figure), and perhaps more rigorously, the one for x_c = 177 cm^{-1} too. Furthermore, in following the line of arguments given in the previous subsection, these results not only confirm the existence of the first concentration threshold (FCT) at the doping concentration of 1.5 wt. % Fe_2O_3, as predicted to lie between this point and 2.2 wt. % Fe_2O_3 by XRD plus structure refinement. The second concentration threshold (SCT) can also be determined at 3.3 wt. % Fe_2O_3, within the given absolute accuracy (doping concentration increments of $\Delta \approx$ 3.3 wt. % Fe_2O_3). Such inference agrees with the fundamental fact that the SCT should lie close to the limit of chemical solubility.[14,18,24] Also, this information can only be extrapolated from the reduced samples, noticing that no clean trends or 'well-behaved' curves were obtained neither for the oxidized or the untreated samples, Figure 7(c). Thus, the application of post-thermal treatment in a reducing atmosphere is not only essential to avoid possible misfits in the interpretation of XRD patterns, see Figure 1c and derived discussion, but also to have more elements in hand for a deeper understanding of the dynamics behind the defect structure of LN:Fe.[37] Reduced LN:Fe could also be of use for applications, specifically in the development of new generation materials for nonlinear optics.

2.2. SHG response

The SHG response from the zero, lowest, intermediate and highest concentration of Fe doping samples under their powder form was then obtained. The complete set of analyzed data is put

at reach in the attached Supporting Information file along with a short video showing the strong sensitivity of sample 45LN:Fe-re to the applied magnetic field (MF). A not too strong applied MF may effectively alter the SHG response from LN:Fe powders. Figure 8 displays the obtained results for the reduced pristine samples. Depth-SHG-intensity profiles were recorded where the fundamental beam focus is translated from air into the powder. Then, two crossed-polarization plots of the SHG intensity recorded at z = 0, both in the absence (black, grey data points) and presence (blue, red data points) of the MF, see Figures 8(b)-(c). The z = 0 depth is here defined as the maximum intensity of the SHG depth profile.

The nonlinear polarization for a non-centrosymmetric material is of electric dipole origin. Higher order terms like the quadrupole electric and dipole magnetic nonlinear polarization contributions can be neglected if the crystal structure is assumed to remain non-centrosymmetric after metal doping and post-thermal treatment.[40] To be noted though, the continuous relaxation of the crystal structure observed for the reduced samples, see Figure 2(a) may to some extent leave open for further discussion the possibility of having an evolving system which becomes more symmetric as the doping concentration increases. Thus, the origin of SHG in the present LN:Fe powders is essentially of electric dipole character. It is thus expected that the material orientational randomness drives the SHG response and that the ferro-magnetic/electric properties provides a minor contribution.

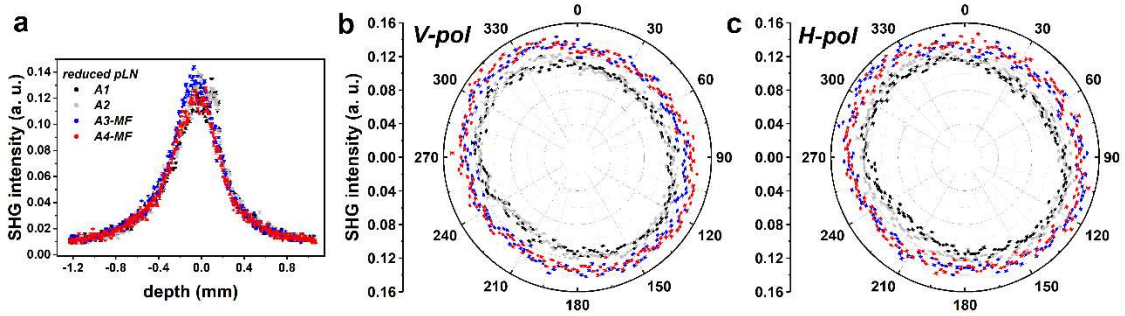

Figure 8 : *(a) SHG intensity depth profiles for sample pLN-re, b) Polar plot of the Vertically polarized SHG intensity as a function of the angle of polarization of the fundamental beam collected at depth z = 0 and (c) Polar plot of the Horizontally polarized SHG intensity as a function of the angle of polarization of the fundamental beam collected at depth z = 0. Blue and red points correspond to the data collected after application of the constant magnetic field whereas black and grey ones correspond to the data collected prior to the application of*

the constant magnetic field. The angular entries of the polar plots describe the input polarization angle respect to the Vertical polarization configuration.

The polar plots shown in Figure 8 exhibit a constant response at z=0 irrespective of the incident linear polarization state of light, detection configuration and application of the MF. Similar SHG intensity depth profiles and polarization plots were obtained for samples pLN and pLN-ox. The observed polarization graphs exhibiting circular plots or constant SHG as a function of the fundamental beam polarization result from the random nature of the granular medium from the optical point of view. Scattering, including single and multiple events leads to the complete loss of the polarization state of the emerging photons at the harmonic frequency. It is however concluded that in this system, centrosymmetry due to the random nature of the powder is not perfect and appears broken. Hence, a net non-zero SHG response can still be observed. This imperfect cancelation of the many single powder grain dipolar contribution cannot be reached because of the combination of imperfect random orientational organization, differences in size and chemical composition from nano-grain to nano-grain. The same arguments could be used to explain the observed differences in the SHG efficiency for larger polycrystalline LN grains of about 2 μm in size made of several aggregated nanocrystals.[39] It is also worth mentioning that the polar plots reported in Figure 8 do not reproduce the results reported in Ref. 15 where more pronounced two-lobes polarization patterns were observed for pristine LN powders of stoichiometric composition at equivalent physical instances of z = 0. This feature may be ascribed to a different relative efficiency in the collection of photons that undergo linear scattering events, the so-called multiply scattered photons, as opposed to almost no linear scattering events, the so-called ballistic photons. In the present case, the contribution from the multiply scattered photons dominates resulting in close to undistorted circular polarization plots.[15]

Sample 8LN:Fe-re exhibits to the contrary an important residual polarized SHG intensity with a clear two-lobe patterns, see Figure 9. Therefore, the powder nano-grains illuminated during the SHG intensity depth profiles and their corresponding polarization plots appear to preserve some orientational order. This feature may occur due to the presence of intrinsic ferroelectric domains. Interestingly, this initial orientational ordering characteristics appears to be modified with the introduction of the magnetic field as seen through the changes in polarization, see Figure 9(b)-(c). Also, interestingly, the application of the MF does change the polarization plots, but does not change the SHG intensity depth profiles. The latter SHG intensity depth

profiles are also much narrower. Pristine LN powders are colorless or white regardless of post-thermal treatment whereas the untreated and oxidized LN:Fe samples are, respectively, pink and orange to the naked eye. Hence, absorption and multi-photon absorption processes also alter the relative weight between detected ballistic and multiply scattered photons. The mean free path of the latter in the sample is longer. Comparison between the SHG intensity depth profiles of samples 8LN:Fe-re in Figure 9(a) and sample pLN-re in Figure 8(a) shows that that this feature induces a collected intensity at z = 0 depth of the SHG intensity maximum is much weaker in the former case.

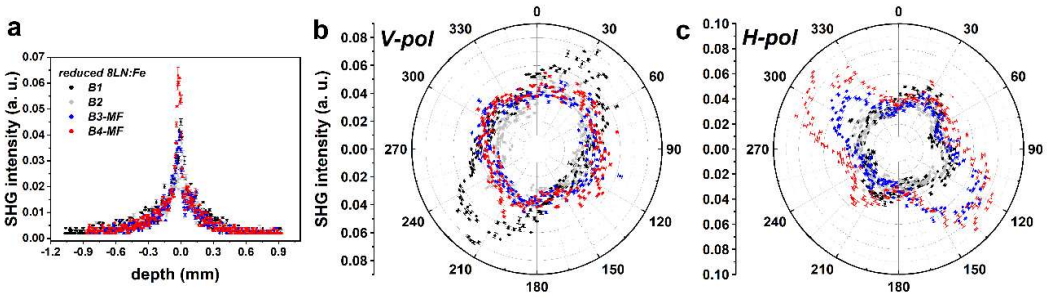

Figure 9 : *(a) SHG intensity depth profile for sample 8LN:Fe-re. b) Polar plot of the Vertically polarized SHG intensity as a function of the angle of polarization of the fundamental beam collected at depth z = 0. c) Polar plot of the Horizontally polarized SHG intensity as a function of the angle of polarization of the fundamental beam collected at depth z = 0. Blue and red points correspond to the data collected after application of the constant magnetic field whereas black and grey ones correspond to the data collected prior to the application of the constant magnetic field. The angular entries of the polar plots describe the input polarization angle respect to the Vertical polarization configuration.*

Figure 10 shows the obtained results for the sample of intermediate Fe doping concentration, that is, sample 22LN:Fe-re. Polarization distortions observed for already for sample 8LN:Fe-re persist although they present now a different behavior. Before application of the constant MF, the polarization plots show some initial ordering although not complete. In the presence of the applied MF, the polarization are modified and appears to tend to a more organized system with a more defined polarized SHG response.

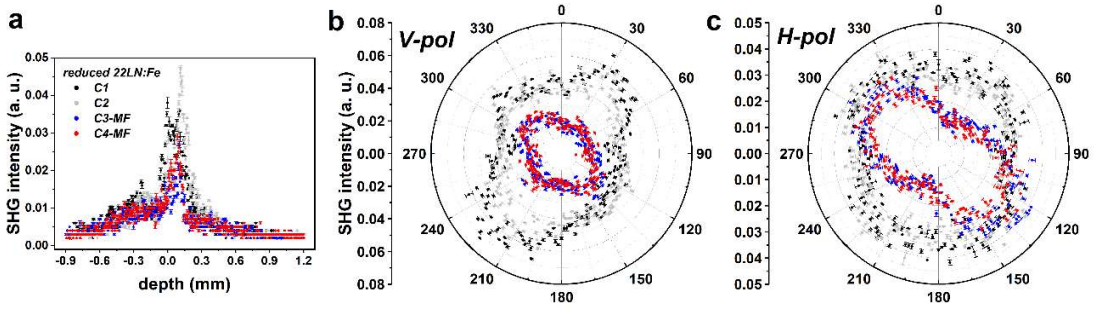

552

553 **Figure 10 :** *(a) SHG intensity depth profile for sample 22LN:Fe-re. b) Polar plot of the*
554 *Vertically polarized SHG intensity as a function of the angle of polarization of the*
555 *fundamental beam collected at depth z = 0. c) Polar plot of the Horizontally polarized SHG*
556 *intensity as a function of the angle of polarization of the fundamental beam collected at depth*
557 *z = 0. Blue and red points correspond to the data collected after application of the constant*
558 *magnetic field whereas black and grey ones correspond to the data collected prior to the*
559 *application of the constant magnetic field. The angular entries of the polar plots describe the*
560 *input polarization angle respect to the Vertical polarization configuration.*

561

562 Thus, it is observed that at this doping concentration rate, re-orientation affects the orientation
563 distribution of the powder nano-grain. This feature can be suggested as a potential mechanism
564 to optimize the SHG response from randomly oriented grains. Also, the SHG intensity depth
565 profile appears rather unsymmetrical with a slow increase and a plateau in the SHG intensity
566 as a function of depth. This feature further underlines the possible role of the MF. Figure 11
567 reporting another run with this sample shows an important SHG signal enhancement and more
568 dramatic changes in the polarization plots. Furthermore, run B in this series of experiments.
569 This shows a strong alignment effect upon application of the external MF on the nano-grains
570 powder. Therefore, the SHG response appears to be tailored by control of the numbers of
571 intrinsic and extrinsic point defects within the hosting pristine structure and thereby setting
572 the magnetization to an optimal value using doping concentration rates between 0.8 and 2.2
573 wt. % Fe_2O_3.

574

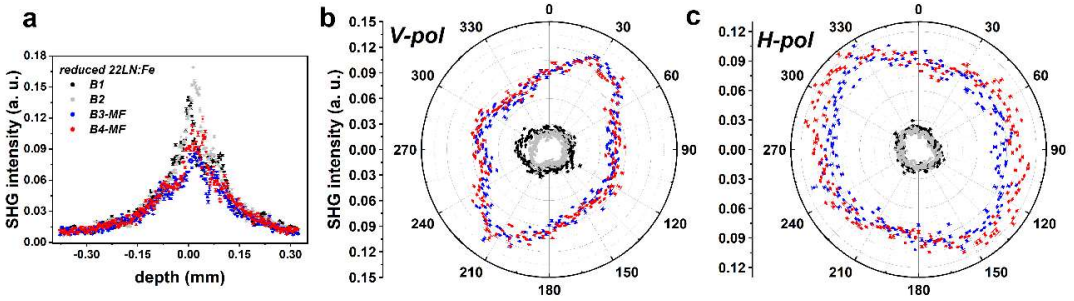

Figure 11 : *(a) SHG intensity depth profile for sample 22LN:Fe-re, second run. b) Polar plot of the Vertically polarized SHG intensity as a function of the angle of polarization of the fundamental beam collected at depth z = 0. c) Polar plot of the Horizontally polarized SHG intensity as a function of the angle of polarization of the fundamental beam collected at depth z = 0. Blue and red points correspond to the data collected after application of the constant magnetic field whereas black and grey ones correspond to the data collected prior to the application of the constant magnetic field. The angular entries of the polar plots describe the input polarization angle respect to the Vertical polarization configuration.*

Photo-induced change in the material seems to be another mechanism to be considered in the overall SHG response of the samples. This is more clearly seen for sample 45LN:Fe-re, see Figure 12. The recorded profiles are no longer invariant for repeated profiles. The SHG intensity almost entirely collapses into a baseline eventually. Polarization distortions are still discernible too, but they are neither well resolved nor reproduced from sample preparation to sample preparation. In this case, the incident fundamental beam is continuously transforming the material over time. Such photo-induced changes can be qualitatively explained in terms of the photo-refraction process. Photo-refraction is the process whereby an inhomogeneity in the refractive index is optically induced. It is characteristic of most insulators, and regularly, the irreversible change is generated by applying intense-laser light.[14] LN is a photorefractive material by excellence. Accordingly, an irradiance as low as 20 $W.cm^{-2}$ at a wavelength of 532 nm is enough for its manifestation in a congruent crystal.[41] Photo-refraction in LN can be either suppressed or enhanced by proper elemental doping. In the latter case, mainly transition metals are employed and some of the devised applications are holography storage, beam coupling, information processing, and computation. Iron has been considered for a long time the strongest photovoltaic-active impurity.[14, 42-43] Thus, although the input power was kept fixed for all experiments performed in this investigation, the sample 45LN:Fe-re is more

susceptible to optical damage simply because it supports more iron in its structure, combined with the fact that the population of oxygen vacancies is at large values as well.

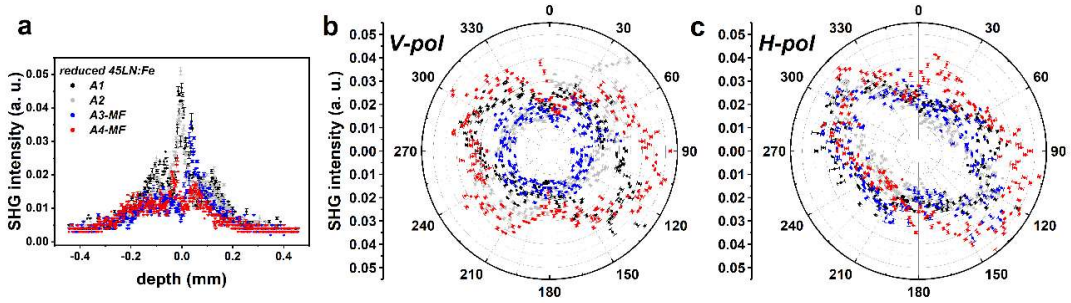

Figure 12 : *(a) SHG intensity depth profile for sample 45LN:Fe-re, second run. b) Polar plot of the Vertically polarized SHG intensity as a function of the angle of polarization of the fundamental beam collected at depth z = 0. c) Polar plot of the Horizontally polarized SHG intensity as a function of the angle of polarization of the fundamental beam collected at depth z = 0. Blue and red points correspond to the data collected after application of the constant magnetic field whereas black and grey ones correspond to the data collected prior to the application of the constant magnetic field. The angular entries of the polar plots describe the input polarization angle respect to the Vertical polarization configuration.*

In contrast, samples 45LN:Fe and 45LN:Fe-ox do not show significant photo-induced changes. In 45LN:Fe-re, the innumerable coexistence of oxygen vacancies and Fe^{3+} ions promotes charge transport and trapping phenomena, main factors at play in photo-refraction. Lastly, in the polarization plots of the SHG response of the untreated and oxidized samples, weak distortions can be seldom traced. The same can be said for the doping concentration of 2.2 wt. % Fe_2O_3. Nevertheless, for practical purposes, samples 22LN:Fe, 22LN:Fe-ox, 45LN:Fe and 45LN:Fe-ox can be assumed to be random or granular from the optical point of view, just as the pristine LN samples are. The application of a post-thermal treatment in a reducing atmosphere thus gives a deeper insight into some fundamental science problems in LN:Fe, but it also entails a modification of some of its intrinsic capabilities in the realm of nonlinear optics.

CONCLUSION

In this work, SHG intensity depth profiles and polarization analysis of iron doped LN powders are performed for several iron doping rates. The powders all exhibit similar SHG

intensity profiles driven by the competition between the Gaussian beam focus translation into the powder from the air side providing SHG signal increase and multi-scattering with possibly absorption leading to the loss of the SHG signal. The powders appear generally randomly oriented, especially for the undoped and weakly doped ones with indication of a weak remaining order possibly due to the ferroelectric property of LN. As the iron doping rate is increased, changes in the polarization graphs upon application of the static magnetic field are observed. Finally, at the highest doping rates, photo-refractive effects are observed. From the measurements on all samples, the following conclusions can therefore be observed :

- For a given doping concentration (zero concentration included), the untreated and oxidized samples present an SHG response of comparable intensity whereas the intensities for their corresponding reduced samples are about one order of magnitude weaker,
- SHG intensity depth profiles are slightly asymmetric correspondingly to a rise obeying wave propagation of a TEM_{00} Gaussian beam along the z-optical axis, at negative z values, and a more rapid decay resulting from convolution between the same propagation phenomena and exponential decay due to the strong optical extinction and scattering, including multiple scattering, at positive z values,
- No material degradation was noticed from the invariance of the repeated four recorded profiles within a given set of experiments,
- SHG intensity depth profiles were not modified upon the application of the MF, and the definition of the $z = 0$ depth through the maximum of the SHG intensity is the same, independently of the presence or absence of the MF.

Post-thermal treatment in a reducing atmosphere is essential for a deep understanding of the static and dynamic characteristics of defect complexes in iron-doped lithium niobate (LN:Fe) powders. It could also enable the development of a new generation characterization tool of random or granular media based on nonlinear optics. Some specific aspects described in the discussion of results should be addressed for formal explication, such as the origin of apparent order in reduced LN:Fe powders before application of the magnetic field (probable due to the intrinsic ferroelectricity in bulk LN) or its apparent lost after a first run of polarization analysis (again, without application of the magnetic field), where loss of polarization information due to multiple scattering of the SHG photons has been neglected here based on arguments related to the inferred absorption properties of the studied materials.

EXPERIMENTAL SECTION

Synthesis: high purity lithium carbonate (Li_2CO_3) and niobium pentoxide (Nb_2O_5), from Alpha Aesar, were used as starting reagents in 1:1 molar ratio. The respective masses of the precursors were determined such that 3 g of congruent lithium niobate was produced, in principle, from the following balanced chemical equation:

$$Li_{1.9}CO_3 + Nb_{2.02}O_5 \rightarrow 2Li_{0.95}Nb_{1.01}O_5 + CO_2, \quad (1)$$

where the most widely accepted defect model to describe congruent solid solutions of LN has been taken into consideration, the lithium vacancy model. The heterogenous mixture of the precursors is then mechanically activated using a high-energy milling process carried out in a SPEX SamplePrep 8000M Mixer/Mill (New Jersey, USA), using nylon vials with yttria-stabilized zirconia (YSZ) balls; a powder-to-ball mass ratio of 0.1 was used for each sample preparation. The milling was performed in 30 min cycles 30 min pauses, to avoid excessive heat inside the milling chamber until 180 min of effective milling time was reached. The resultant activated powders were then isothermally calcinated in an air atmosphere at 850 °C for 180 min, using a tubular GSL1100X furnace (MTI Corporation, USA); no ramp was used, and the samples were cooled down slowly to RT. High-quality, pure ferroelectric LN powders with a near—congruent chemical composition are obtained at this stage of synthesis, as confirmed by X-Ray Diffraction (XRD) and Raman Spectroscopy: the combination of characterization techniques gives an averaged ratio Li:Nb = 48.9:51.1 (the congruent point is described by the ratio Li:Nb 48.5:51.5). The steps described so far are repeated several times (characterizations included) to produce enough mass of pristine powder, which would be later doped with Fe ions as it is described in the following paragraph.

In the doping stage of synthesis, heterogeneous mixtures of pristine LN and commercial Fe_2O_3 (Alpha Aesar, Puratronic 99.998 %) were made with different rates: 0.8, 1.5, 2.2, 3.3, 4.5, and 6.0 wt. % Fe_2O_3. Mixing, homogenization of particle size distribution, and lowering of surface energy are simultaneously obtained after milling with the SPEX SamplePrep 8000M Mixer/Mill (New Jersey, USA) for an effective time of 60 min. Then, doping of Fe ions was carried out through diffusion after calcination for 60 h at 850° (air atmosphere). The resultant materials are labeled as it follows: 8LN:Fe, 15LN:Fe, 22LN:Fe, 33LN:Fe, 45LN:Fe and 60LN:Fe. During the final stage of synthesis, reduction and oxidation treatments were

performed for 60 min at 850 °C in controlled atmospheres of ultra-high purity hydrogen and oxygen, respectively.

Characterization: the XRD patterns of all the samples were recorded in the air at RT using a Panalytical X-Pert system (Almelo, The Netherlands) with the Bragg-Brentano θ-θ geometry, a radiation source of CuKα (λ=1.54 $\dot{A}$), a Ni 0.5% CuKβ filter in the secondary beam, and a 1-dimensional position-sensitive silicon strip detector (Bruker, Linxeye, Karlsruhe, Germany). The diffraction intensity, as a function of the 2θ angle, was measured between 10.00° and 80.00°, with a step of 0.016° every 30 s. Structural refinements by the Rietveld method were performed using the computational package X'Pert HighScore Plus from PANalytical, version 2.2b (2.2.2), released in 2006.[44] Diffraction data for phases $LiNbO_3$ (COD 2101175), hematite-Fe_2O_3 (JCPDS PDF 04-015-6943), and α-Fe (JCPDS PDF 00-006-0696) were used from the Crystallography Open Database and the Powder Diffraction File (ICDD®), respectively.[19,21] In the determination of the averaged crystallite sizes, a lanthanum hexaboride (LaB_6) single crystal was used in this case as the standard sample, refined with the diffraction data available in the ICSD-194636 card (FIZ Karlsruhe, Germany). The analysis by X-Ray Photoelectron Spectroscopy (XPS) was performed in a spectrometer equipped with AL kα (1486.7eV) monochromator, and a detector 1D DLD with analyzer Phoibos 150. The electron energy analyzer is operated with a pass energy of 15 eV. The used step size is 0.1 eV and the powders were deposited on Cu on Mo tape. The binding energy of the peak C 1s 284.8 eV was used as reference for calibration.

The structural evolution of all samples was also analyzed by Raman Spectroscopy. Unpolarized Raman spectra were recorded in the air using a WITec confocal Raman microscope (Alpha 300R, Germany) with a 532 nm source of excitation wavelength (continuous wave diode laser) and 2-3 cm^{-1} of spectral resolution. A CCD detector (cooled to -60 °C) was used to collect Stokes Raman signals in a backscattering configuration under a 0.4NA:20x objective lens (ZEISS, Germany). With this equipment, spectra were recorded over the wavenumber range 100-3600 cm^{-1} at RT, the light being incident on the normal component of the sample with a power of 0.50 mW.

Depth profiling and polarization-resolved SHG: A picosecond laser (EKSPLA PL2231-50-SH/TH Nd:YAG pulsed laser System, University Laboratory of Optics at Surfaces (Laboratorio Universitario de Óptica de Superficies) into the Physics Institute of UNAM

(LOS-UNAM)) delivering 26 ps pulses at a repetition rate of 50 Hz was used as the source of light for excitation. The fundamental wavelength was set to 1064 nm and no resonance features were observed. The laser beam was then passed through a half-wave plate (HWP) and polarizing cube to select the linear input polarization angle as well as for precise control of the input power. For control and automation purposes, a reference arm is generated from the reflected light at a transparent slide placed on the beam propagation with arbitrary orientation, it is aimed toward a Thorlabs DET 10A fast photodiode coupled to a Tektronix MSO 4034 Oscilloscope (USA). The transmitted light defines the experimental optical axis. Depth-SHG-intensity profiles result from z-sectioning the SHG response of the samples along the optical axis; a microscope-like experimental setup was constructed on a vertical plane for this purpose. At the entrance, the light at the fundamental wavelength propagates downwards, it first passes through a filter to reject any unwanted harmonic light ($\lambda_{SHG} \approx 532$ nm) and then through an HWP mounted on a motorized rotation stage. A long-pass dichroic mirror follows (650 nm Cut-On), positioned about 45 degrees with respect to the optical axis. The excitation beam keeps propagating unaltered until it enters a 0.25NA:10x objective lens (Newport, USA), and afterward, it impinges from the top into the powders being supported on a microscope coverslip. The objective lens is mounted on a motorized linear-translation stage with a minimum incremental step of 0.05 μm, which allows probing of the nonlinear optical response at several experimental conditions, distinguishing between pre-focal ($z<0$, beam waist in air medium), focal ($z=0$, beam waist at the air/powder interface) and post-focal excitation conditions ($z>0$, the physical instances for which a hypothetical undistorted propagation would lead to focused beam penetrating the sample). On the other hand, considering the stage just before the light beam enters the objective lens, all the experimental procedures of this investigation were done at a fixed input power of (1.65 ± 0.01) mW. The value represents the weighted average of several independent measurements carried on routinely once or twice per day in a 2–3-week time interval.

The harmonic light from within the powders and from the air/powder interfaces propagates randomly in all possible directions. Depending on the used objective lens and the scattering properties of the samples, a given fraction of the harmonic light backscatters, or is retro-reflected into the objective lens. It propagates upwards along the optical axis until reaching the dichroic mirror, where its wavevector rotates close to 90 degrees. A long-pass filter is placed on the propagation line to reject any fundamental light (if leaked from the dichroic mirror). A set of three “blue” mirrors (with high reflectance at $\lambda_{SHG} \approx 532$ nm) is employed to

765 reset the propagation axis on a horizontal plane and direct it toward the detection stage. The
766 latter is composed of an analyzer (HWP plus polarizing cube) and a monochromator
767 (Princeton Instruments, Acton SP2300, USA) coupled to a photo-multiplier tube (PMT,
768 Hamamatsu H5784-04, Japan) working in the photon counting regime; the output signal is
769 decoded with the digital oscilloscope (Tektronix). A biconvex lens (f=150 mm) was used to
770 focus the harmonic light at the entrance of the monochromator which was held operating at a
771 fixed spectral position of 532 nm for all instances.
772
773 The cubic polarizer sets the detected light as linearly polarized and parallel to the horizontal
774 plane defining the cross section (or top surface) of the optical table. In what respects the
775 detection stage, the zeroth or original configuration is defined by putting the HWP fast-axis
776 perpendicular to the transmission axis of the polarizer, that is, parallel to the normal
777 component of the top surface of the optical table. It will be hereafter referred to as V-pol (V
778 stands for vertical). The horizontal H-pol configuration is also of interest –only in the
779 polarization analysis of the SHG response: it can be easily obtained by clockwise rotating the
780 HWP by θ_{HWP} = 45° ($\theta_{pol.\ angle}$ = 90°). All the recorded intensity depth profiles were obtained
781 using the zeroth-zeroth experimental configuration, namely, the V-pol configuration at the
782 detection stage plus the setting of the first HWP (excitation stage, fundamental wave) at
783 position $\theta_{HWP} = \theta_{pol.\ angle}$ = 0°. The scanning resolution in the depth profiling was set to either
784 5 μm or 2 μm, depending on the optical absorption properties of the samples: wide profiles
785 (untreated and oxidized powders) or narrower profiles (reduced powders). Recall that strong
786 absorbance in the visible regime could be interpreted as a lower probability of the harmonic
787 photons being retro-reflected and re-inserting the objective lens, that is, a shortened detection
788 efficiency (narrower profiles).
789
790 A polarization analysis of the SHG response conveys an effective in-plane rotation of the
791 linear polarization state of the fundamental wave impinging on the samples. A full range
792 analysis (0-360°) can be effectuated by rotating the first HWP in a 0-180° range. It is done in
793 the present investigation regarding all the polarization-resolved SHG experiments, with a
794 resolution on the polarization angle of 2° (the incremental step used in every experiment was
795 of $\Delta\theta_{HWP}$ = 1°). Signal detection is done in the same fashion as for the case of the depth
796 profiles, but now using both configurations, V-pol first and H-pol afterwards. These
797 polarization-resolved measurements are done at the physical instance of maximum SHG

intensity, by the setting of the motorized linear-translation stage in such position (defined as z = 0).

The procedure was performed three times for each studied sample so that three distinct points are probed randomly from the same sample (runs A, B, and C). In each sample preparation after the first one, the recently studied sample is recovered back into its container and recombined with the rest of the synthesized powder. Before studying the SHG response of the same powder for a second or third time, the powder was systematically chopped with a coverslip to cancel out any possible orientation of grains induced by the applied MF in the previous set of experiments. In this instance, only the pristine samples (pLN) and doped samples 8LN:Fe, 22LN:Fe, and 45LN:Fe were studied; the three available states of oxidation were considered (untreated, oxidized, and reduced samples), so that a total of 36 independent sets of experiments were performed.

Supporting Information

Supporting Information is available from the Wiley Online Library or from the author.

Acknowledgements

This research was partially funded by Universidad Autónoma de Ciudad Juárez, ECOS-Nord CONACyT-Anuies 315658-M20P02 (Mexico-France) and PAPIIT-UNAM IN112022. M.J.G.-R. and O.A.V.-C. thank CONACyT scholarship grant. J.A.R.E. thanks sabbatical funding from PASPA-UNAM, CONACyT and University of Sherbrooke. The authors wish to acknowledge the technical assistance of Gerardo Daniel Rayo López, Lorena Rivera Rios, and Manuel Aguilar Franco. Special thanks to Edwin Abad Vela for his help in editing the ToC figure and producing the Supporting Information media (video).

Received: ((will be filled in by the editorial staff))

Revised: ((will be filled in by the editorial staff))

Published online: ((will be filled in by the editorial staff))

REFERENCES

[1] S. Troiler-McKinstry, *Am. Cer. Soc. Bull*. **2020**, *99*, 22.

[2] O. Sánchez-Dena, C. D. Fierro-Ruiz, S. D. Villalobos-Mendoza, D. M. Carrillo-Flores, J. T. Elizalde-Galindo, R. Farías, *Crystals* **2020**, *10*, 973.

[3] a) D. N. Nikogosyan, *Nonlinear Optical Crystals: A Complete Survey*, Springer, NY, USA **2005**; b) R. W. Boyd, *Nonlinear Optics*, Academic Press, Rochester, NY, USA **2008**.

[4] a) L. Yang, Y. Zhuang, W. Zhao, X. Liu, Q. Hu, Z. Xu, X. Wei, *Mater. Lett*. **2022**, *308*, 131292; b) N. Amiune, D. N. Puzyrev, V. V. Pankratov, D. V. Skryabin, K. Buse, I. Breunig, *Opt. Express* **2021**, *29*, 41378; c) B. Desiatov, A. Shams-Ansari, M. Zhang, C. Wang, M. Loncar, *Optica* **2019**, *6*, 380; d) C. Pang, R. Li, Z. Li, N. Dong, C. Cheng, W. Nie, R. Böttger, S. Zhou, J. Wang, F. Chen, *Adv. Opt. Mater*. **2018**, 6, 1800357; e) M. Zhang, C. Wang, R. Cheng, A. Shams-Ansari, M. Loncar, *Optica* **2017**, *4*, 1536.

[5] L. Burrows, Now Entering, Lithium Niobate Valley: Researchers Demonstrate High-Quality Optical Microstructures Using Lithium Niobate, https://www.seas.harvard.edu/news/2017/12/now-entering-lithium-niobate-valley, accessed: August, **2022**.

[6] M. Kösters, B. Sturman, P. Werheit, D. Haertle, K. Buse, *Nat. Photonics* **2009**, *3*, 510.

[7] P. F. Brevet, *Surface Second Harmonic Generation*, Presses polytechniques et universitaires romandes, France **1997.**

[8] T. Verbiest, K. Clays, V. Rodriguez, *Second-Order Nonlinear Optical Characterization Techniques,* CRC Press, Taylor & Francis Group, USA **2009**.

[9] S. Lherminier, R. Planet, V. Levy dit Vehel, G. Simon, L. Vanel, K. J. Maloy, O. Ramos, *Phys. Rev. Lett*. **2019**, *122*, 218501.

[10] A. Bérut, H. Chauvet, V. Legué, B. Moulia, O. Pouliquen, Y. Forterrre, *PNAS* **2018**, *115*, 5123.

[11] J. Butet, P.-F. Brevet, O. J. F. Martin, *ACS Nano* **2015**, *9*, 10545.

[12] C. D. Fierro-Ruiz, O. Sánchez-Dena, E. M. Cabral-Larquier, J. T. Elizalde-Galindo, R. Farías, *Crystals* **2018**, *8*, 108.

[13] a) J. M. D. Coey, *Curr. Opin. Solid Mater. Sci*. **2006**, *10*, 83; b) J. M. D. Coey, M. Venkatesan, C. B. Fitzgerald, *Nat. Mater*. **2005**, *4*, 173.

[14] O. Sánchez-Dena, S. D. Villalobos-Mendoza, R. Farías, C. D. Fierro-Ruiz, *Crystals* **2020**, *10*, 990.

[15] O. Sánchez-Dena, Z. Behel, E. Salmon, E. Benichou, J. A. Reyes-Esqueda, P.-F. Brevet, C. Jonin, *Opt. Mater*. **2020**, *107*, 110169.

[16] E. Adler, *Phys. Rev.* **1964**, *134*, A728.
[17] B. Knabe, D. Schütze, T. Junggk, M. Svete, W. Assenmacher, W. Mader, K. Buse, *Phys. Status Solidi (a)* **2011**, *208*, 857.
[18] T. Volk, M. Wöhlecke, *In Lithium Niobate: Defects, Photorefraction and Ferroelectric Switching*, Vol 115, (Eds: R. Hull, R. M. Osgood, Jr. Parisi, H. Warlimont), Springer, Berlin/Heidelberg, Germany **2009**, Ch. 2.
[19] A. Vaitkus, A. Merkys, S. Grazulis, *J. Appl. Cryst.* **2021**, *54*, 661.
[20] O. Sánchez-Dena, C.J. Villagomez, C.D. Fierro-Ruiz, A.S. Padilla-Robles, R. Farías, E. Vigueras-Santiago, S. Hernández-López, J.A. Reyes-Esqueda, *Crystals* **2019**, *9*, 340.
[21] S. Gates-Rector, T. Blanton, *Powder Diffr.* **2019**, 34, 352.
[22] a) P. Lerner, C. Legras, J.P. Dumas, *J. Cryst. Growth* **1968**, *3*, 231; b) H. Donnerberg, S.M. Tomlinson, C.R.A. Catlow, O.F. Schirmer, *Phys. Rev. B* **1989**, *40*, 11909; c) H. Donnerberg,, S.M. Tomlinson, C.R.A. Catlow, *J. Phys. Chem. Solids* **1991**, *52*, 201; d) F.P. Safaryan, R.S. Feigelson, A.M. Petrosyan, *J. Appl. Phys.* **1999**, *85*, 8079.
[23] a) S.C. Abrahams, P. Marsh, *Acta Cryst.* **1986**, *B42*, 61; b) O.F. Schirmer, O. Thiemann, M. Wöhlecke, *J. Phys. Chem. Solids* **1991**, *52*, 185; c) N. Zotov, H. Boysen, F. Frey, T. Metzger, E. Born, *J. Phys. Chem. Solids* **1994**, *55*, 145; d) A.P. Wilkinson, A.K. Cheetham, R.H. Jarman, *J. Appl. Phys.* **1998**, *74*, 3080.
[24] a) L. Kovács, L. Kocksor, É. Tichy-Rács, K. Lengyel, L. Béncs, G. Corradi, *Opt. Mater. Express* **2019**, *9*, 4506; b) L. Kovács, L. Kocksor, Z. Szaller, I. Hajdara, G. Dravecz, K. Lengyel, G. Corradi, *Crystals* **2017**, *7*, 230; c) L. Kovács, Z. Szaller, K. Lengyel, G. Corradi, *Opt. Mater.* **2014**, *37*, 55.
[25] a) Y.-Y. Li, H.-L. Chen, G.-J. Chen, C.-L. Kuo, P.-H. Hsieh, W.-S. Hwang, *Materials* **2017**, *10*, 380; b) Y. Noguchi, R. Inoue, M. Miyayama, *Adv. Conden. Matter Phys.*, https://doi.org/10.1155/2016/2943173; c) F. Zeng, P. Sheng, G. S. Tang, F. Pan, W. S. Yan, F. C. Hu, Y. Zou, Y. Y. Huang, Z. Jiang, D. Guo, *Mater. Chem. Phys.* **2012**, *136*, 783; d) P. Bourson, M. Aillerie, M. Cochez, M. Ferriol, Y. Zhang, L. Guilbert, *Opt. Mater.* **2003**, *24*, 111; e) T. Gog, P. Schotters, J. Falta, G. Materlik, M. Grodzicki, *J. Phys.: Condens. Matter* **1995**, *7*, 6971.
[26] a) G. E. Peterson, A. M. Glass, T. J. Negran, *Appl. Phys. Lett.* **1971**, *19*, 130; b) M. G. Clark, F. J. DiSalvo, A. M. Glass, G. E. Peterson, *J. Chem. Phys.* **1973**, *59,* 6209; c) W. Phillips, D. L. Staebler, *J. Electron. Mater.* **1974**, *3*, 601; d) R. R. Shah, D. M. Kim, T. A. Rabson, F. K. Tittel, *J. Appl. Phys.* **1976**, *47*, 5421.
[27] R. D. Shannon, C. T. Prewitt, *Acta Cryst. B* **1969**, *25*, 925.

[28] X. Kang, L. Liang, W. Song, F. Wang, Y. Sang, H. Liu, *CrystEngComm* **2016***, 18*, 8136.
[29] S. Li, D. Li, S. Li, G. Wang, X. Sun, Li. Xu, H. Yuan, *J. Supercond. Nov Magn.* **2022**, *35*, 2897.
[30] A. Tamilselvan, S. Balakumar, M. Sakar, C. Nayek, P. Murugavel, K. S. Kumar, *Dalton Trans*. **2014**, *43*, 5731.
[31] C. Díaz-Moreno, J. Lopez, J. González-Hernández, R. Escudero, J.L. Heiras, M. J. Yacamán, A. Hurtado-Macias, *J. Magn. Magn. Mater*. **2016**, *407,* 291.
[32] R. Hernández-Molina, J. A. Hernández-Márquez, J. L. Enríquez-Carrejo, J. R. Farias-Mancilla, P. G. Mani-González, E. Vigueras Santiago, J. M. Yáñez-Limón, *Superficies vacío* **2015**,*28*, 115.
[33] M. V. Ciampolillo, A. Zaltron, M. Bazzan, N. Argiolas, C. Sada, M. Bianconi, *J. Appl. Phys.* **2010**, *107*, 084108.
[34] Y. Y. Li, H. L. Chen, G. J. Chen, C. L. Kuo, P. H. Hsieh, W. S. Hwang, *Materials*, **2017**, *10*, 380.
[35] P. C. Graat, M. A. Somers, *Appl. Surf. Sci*. **1996**, *100*, 36.
[36] T. Yamashita, P. Hayes, *Appl. Surf. Sci,* **2008***, 254,* 2441.
[37] a) M. D. Fontana, P. Bourson, *Appl. Phys. Rev.* **2015**, *2*, 040602; b) S. Margueron, A. Bartasyte, A. M. Glazer, E. Simon, J. Hlinka, I. Gregora, J. Gleize, *J. App. Phys.* **2012**, *111*, 104105; c) P. Hermet, M. Veithen, Ph. Ghosez, *J. Phys.: Condens. Matter* **2007**, *19*, 456202; d) V. Caciuc, A. V. Potsnikov, G. Borstel, *Phys. Rev. B* **2000**, *61*, 8806; e) Y. Repelin, E. Husson, F. Bennani, C. Proust, *J. Phys. Chem. Solids* **1999**, *60*, 819; f) R. F. Schaufele, M. J. Weber, *Phys. Rev.* **1966**, *152*, 705.
[38] a) G. Pezzotti, *J. Appl. Phys.* **2013**, *113*, 211301; b) S. Sanna, S. Neufeld, M. Rüsing, G. Berth, A. Zrenner, W. G. Schmidt, *Phys. Rev. B* **2015**, *91*, 224302.
[39] O. Sánchez-Dena, E. V. García-Ramírez, C. D. Fierro-Ruiz, E. Vigueras-Santiago, R. Farías, J. A. Reyes-Esqueda, *Mater. Res. Express* **2017**, *4*, 035022.
[40] N. Bloembergen, R. K. Chang, S. S. Jha, C. H. Lee, *Phys. Rev.* **1968**, *74*, 813.
[41] Y. Kong, F. Bo, W. Wang, D. Zheng, H. Liu, G. Zhang, R. Rupp, J. Xu, *Adv. Mater.* **2020**, *32*, 1806452.
[42] M. Falk, K. Buse, *Appl. Phys. B* **2005**, *81,* 853.
[43] W. Keune, S. K. Date, I. Dézsi, U. Gonser, *J. Appl. Phys.* **1975**, *46*, 3914.
[44] T. Degen, M. Sadki, E. Bron, U. König, G. Nénert, *Powder Diffr.* **2014**, *29*, S13.

Table of Contents Figure

Second Harmonic Generation measurements convey the obtention of intensity depth profiles plus in-plane rotation of the linear polarization state of the light impinging on the samples. Excitation takes place on a vertical plane. Input power does not represent a variable of study, whereas discussion of the results focuses into cases absence/presence of a constant magnetic field about 600 G.

Mónica J. García-Rodríguez, Oswaldo Sánchez-Dena,* Omar A. Velasco-Cortez, César L. Ordóñez-Romero, Milton O. Vázquez-Lepe, Rurik Farías, Pierre-François Brevet, and Jorge A. Reyes-Esqueda

Experimental setup for SHG depth profiling and polarized-resolved analysis.

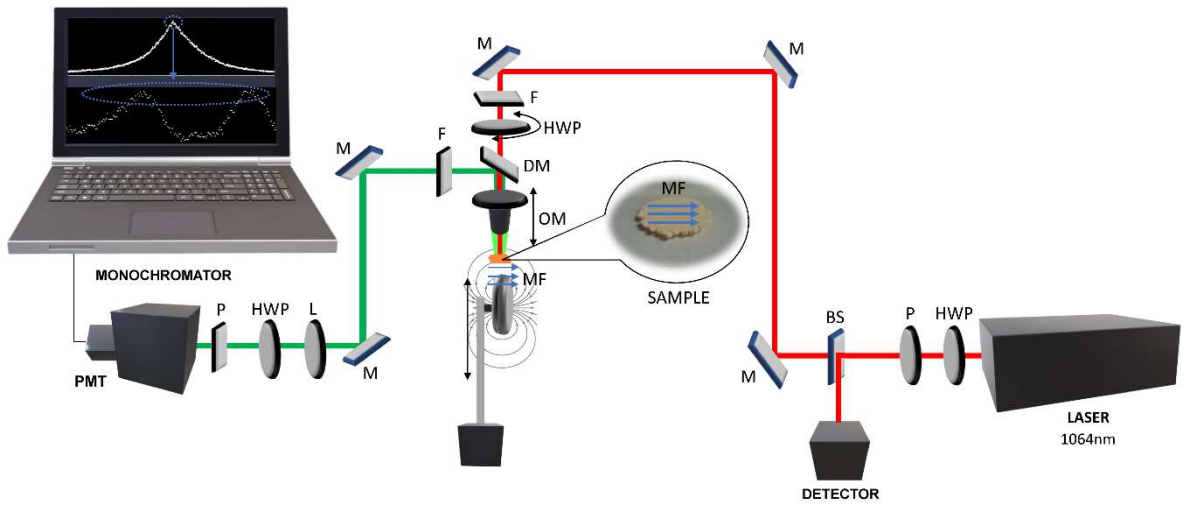

Supporting Information

Synthesis, Characterization, and Second Harmonic Generation of Multiferroic Iron—Doped Lithium Niobate Powders

Mónica J. García-Rodríguez, Oswaldo Sánchez-Dena, Omar A. Velasco-Cortez, César L. Ordóñez-Romero, Milton O. Vázquez-Lepe, Rurik Farías, Christian Jonin, Pierre-François Brevet, and Jorge A. Reyes-Esqueda*

LiNbO3 Crystal Structure

A scheme of the congruent crystal structure of lithium niobate is presented to aid the reader in following the derived discussions in the main document, specifically those corresponding to the results on X-Ray Diffraction and Raman Spectroscopy.

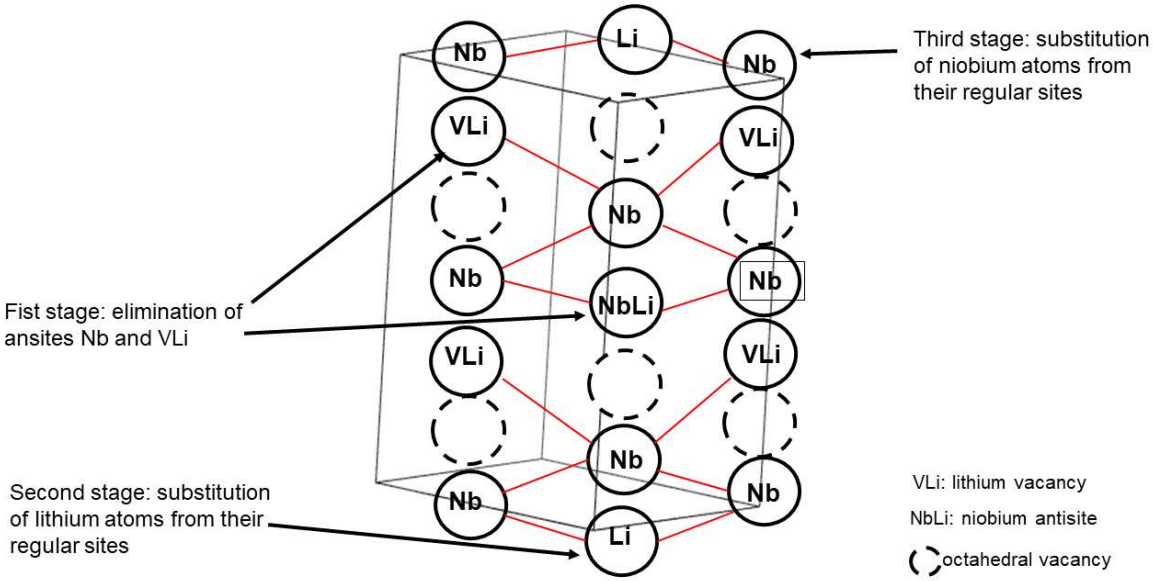

Figure S1. Atomic arrangement for single crystal lithium niobate with congruent chemical composition, showing the discussed dynamics regarding cationic substitution by means of iron doping.

Information in tables

Table S1. 6-fold coordination ionic radii of iron, lithium, and niobium. Reproduced after Shannon and Prewitt (1969).[1]

Ion	Fe^{2+}	Fe^{3+}	Li^{+}	Nb^{4+}	Nb^{5+}
Effective radius [pm]	77.0	64.5	74.0	69.0	64.0

Table S2. Fundamental lattice vibrations of the LN system, as described by Pezzotti (2013) in terms of the relative wavenumber.[2]

Raman shift [cm^{-1}]	Type of vibration
153, 238	deformation of the Nb-O framework
250-400	Li displacements
277	Li-O stretching ⊕ O-Li-O bending
260, 321	O and Li (small) displacements
433	O-Nb-O bending
550-700	O displacement ⊕ Nb-O stretching
877	Nb-O stretching

a) Differences in the Raman shift entries to the original source might be addressed to an overlapping of the longitudinal and transverse components of the polar modes in random media. The given information has been herein adapted according to the resolution of individual bands shown in Figure 6a.

SHG response (complete set of results)

For all the figures given below:

Note: the blue and red points correspond to the data collected after application of the constant magnetic field, namely recording steps 8 to 15, as it is described in the main document. The angular entries of the polar plots describe the input polarization angle respect to the V-pol configuration.

Incises a, b, c: first independent set of experiments for a single point randomly chosen on the sample, or simply run A.

Incises d, e, f: run B.

Incises g, h, i: run C.

Left sides: intensity depth profiles (recording steps 1-black:2-grey:14-blue:15-red).

Centers: V-polar plots collected at maximum SHG intensity or z=0 (recording steps 4-black:6-grey:9-blue:11-red).

Right sides: H-polar plots collected at maximum SHG intensity or z=0 (recording steps 5-black:7-grey:10-blue:12-red).

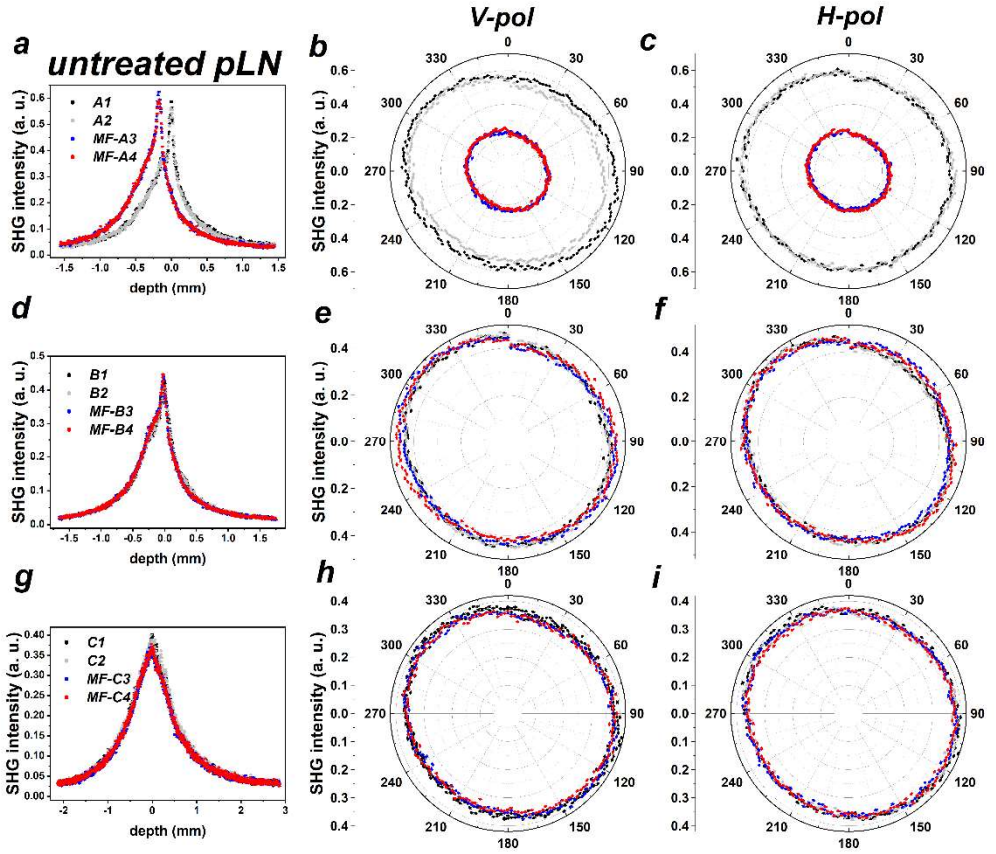

992
993 **Figure S2.** Pristine sample.

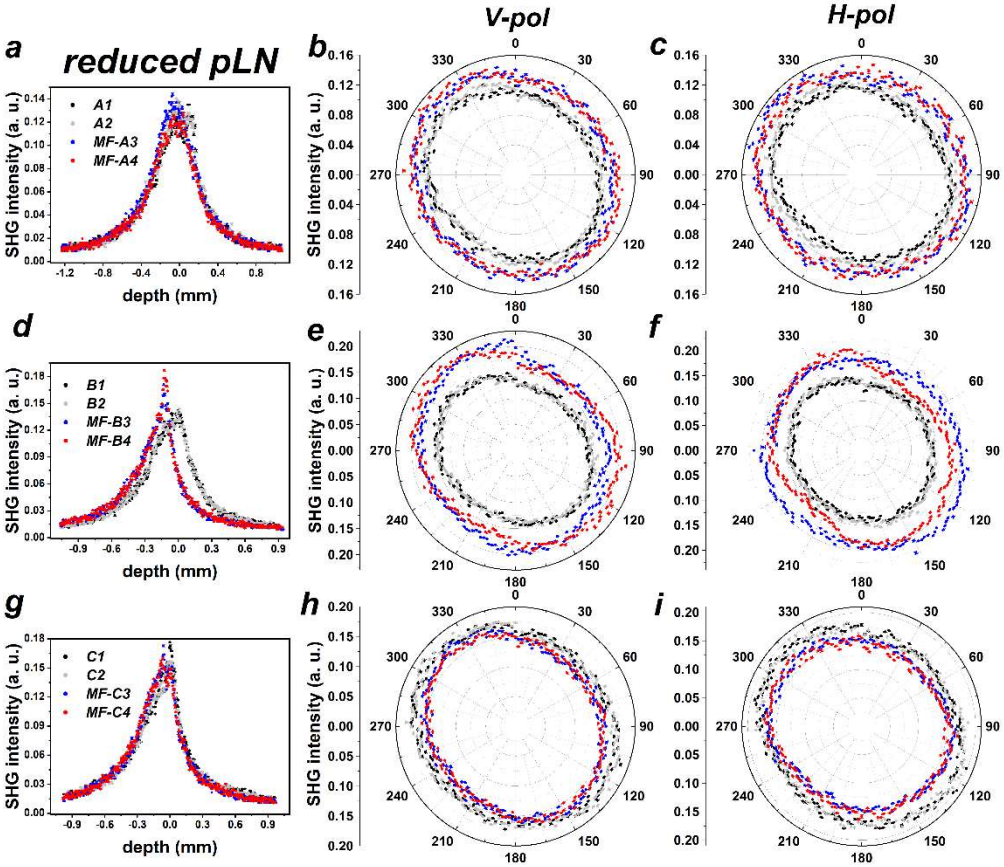

994
995 **Figure S3.** Reduced pristine sample.

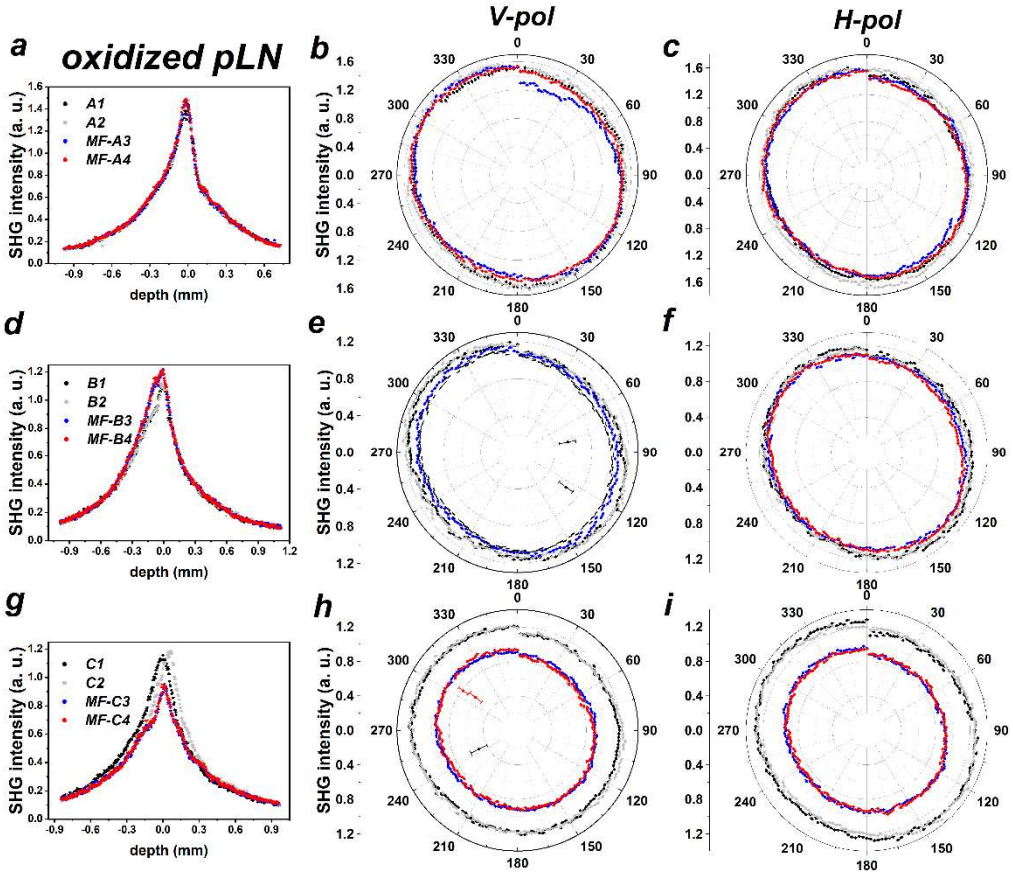

996
997 **Figure S4.** Oxidized pristine sample.

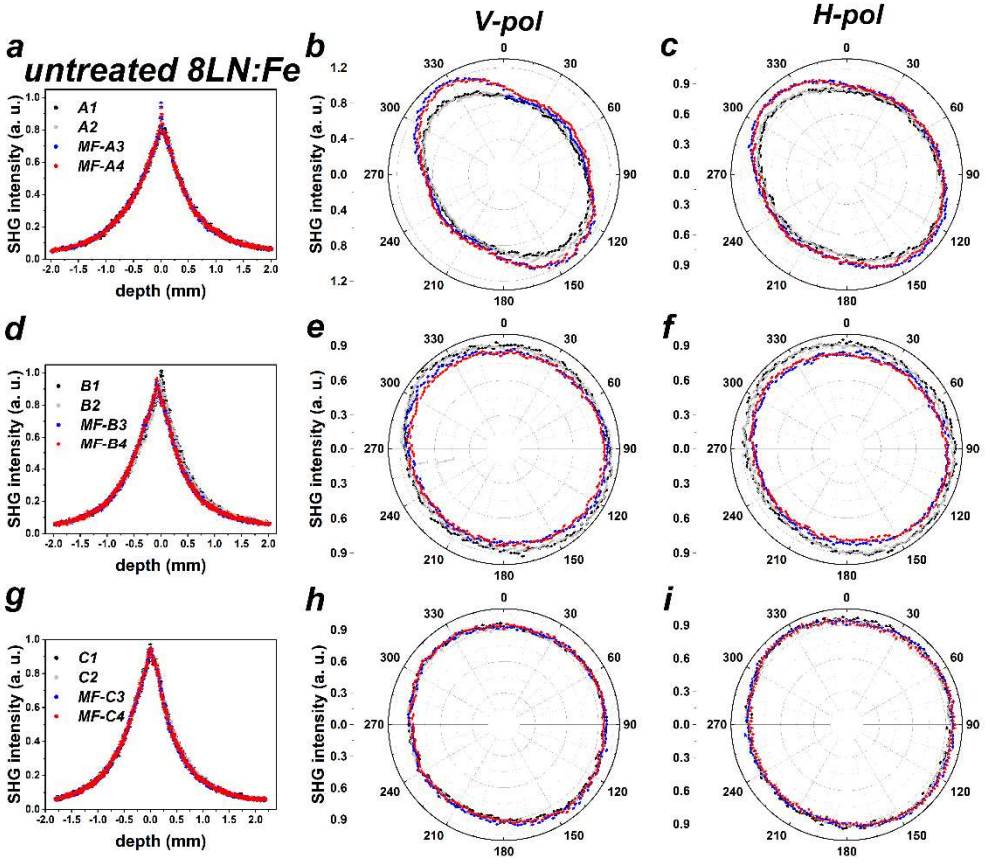

998
999 **Figure S5.** Iron doped $LiNbO_3$ powders with doping concentration of 0.8 wt. % Fe_2O_3.

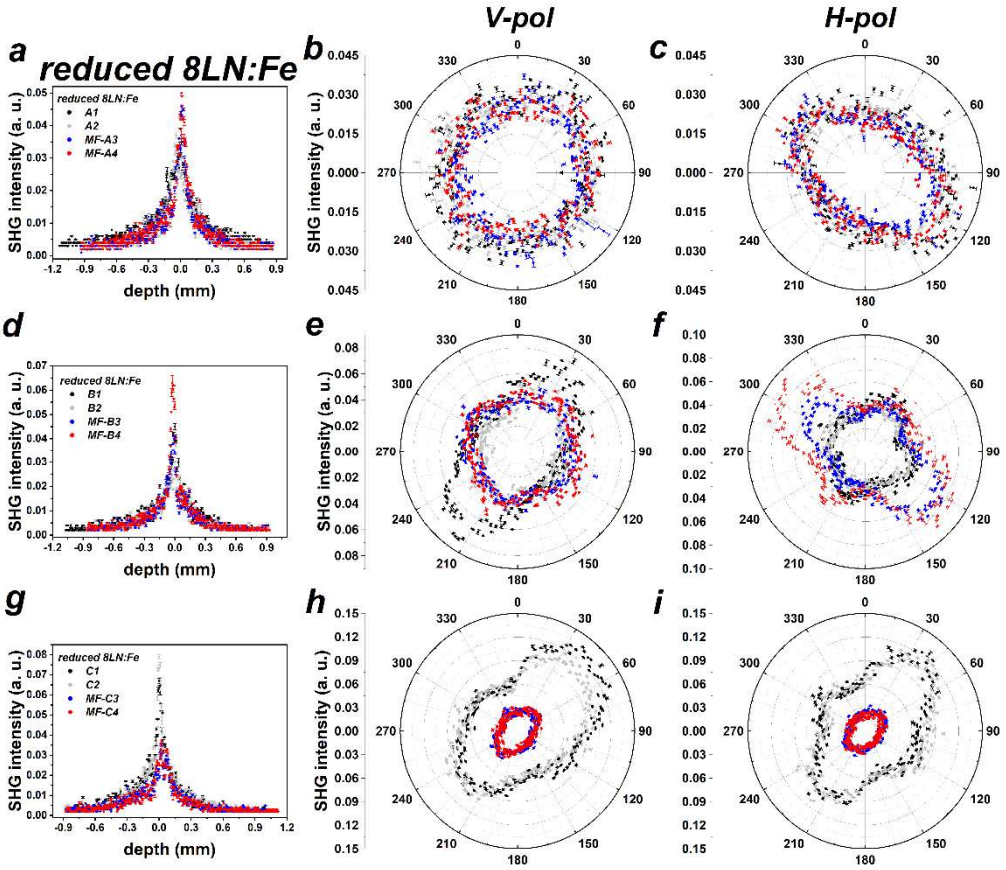

1000
1001 **Figure S6.** Reduced iron doped $LiNbO_3$ powders with doping concentration of 0.8 wt. % Fe_2O_3.

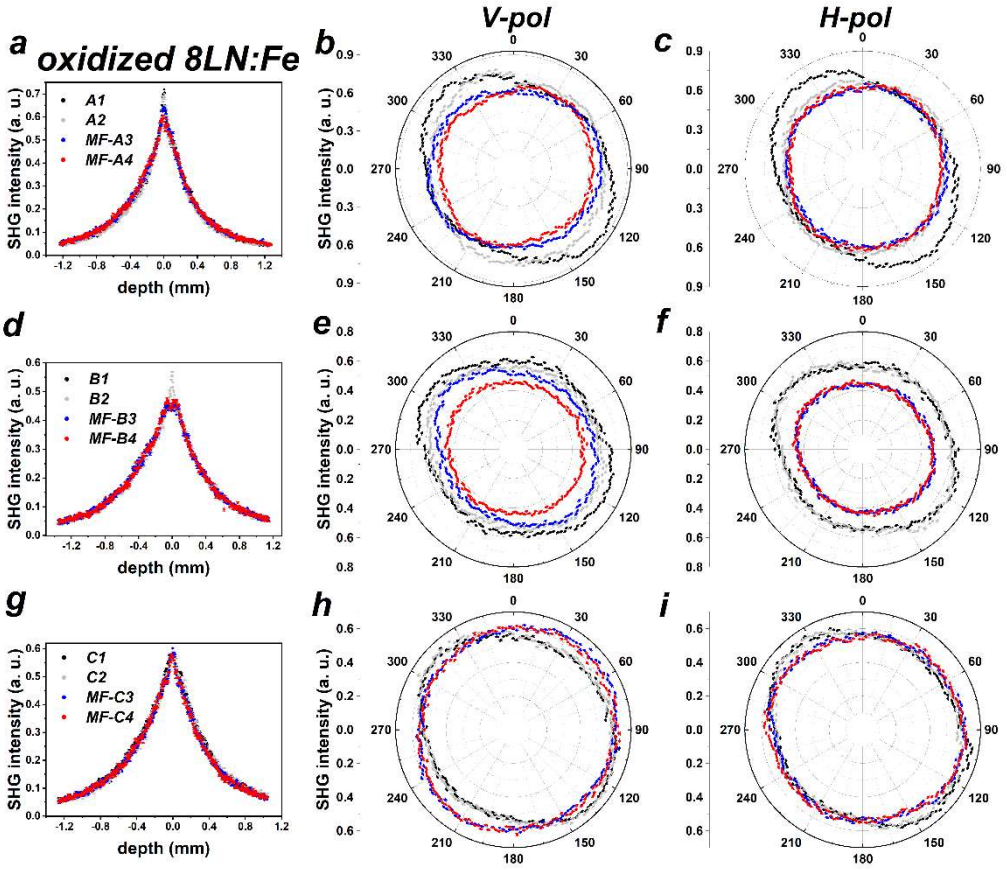

1002
1003 **Figure S7.** Oxidized iron doped $LiNbO_3$ powders with doping concentration of 0.8 wt. % Fe_2O_3.

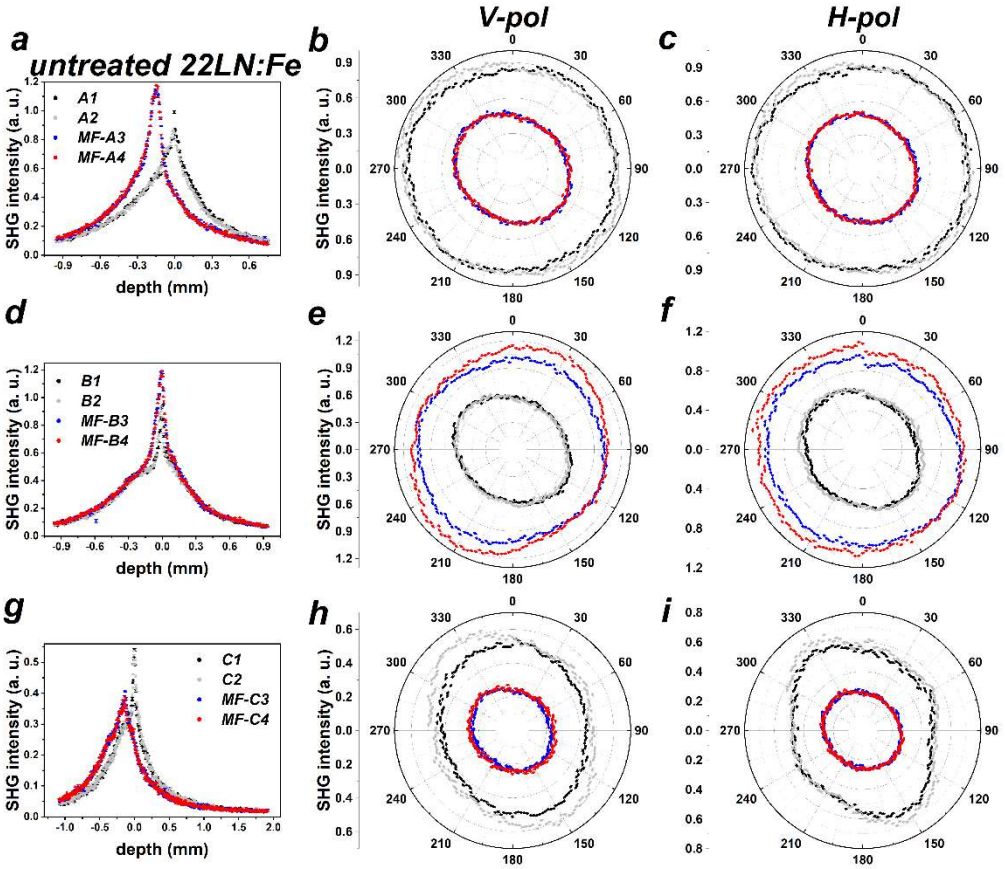

1004
1005 **Figure S8.** Iron doped $LiNbO_3$ powders with doping concentration of 2.2 wt. % Fe_2O_3.

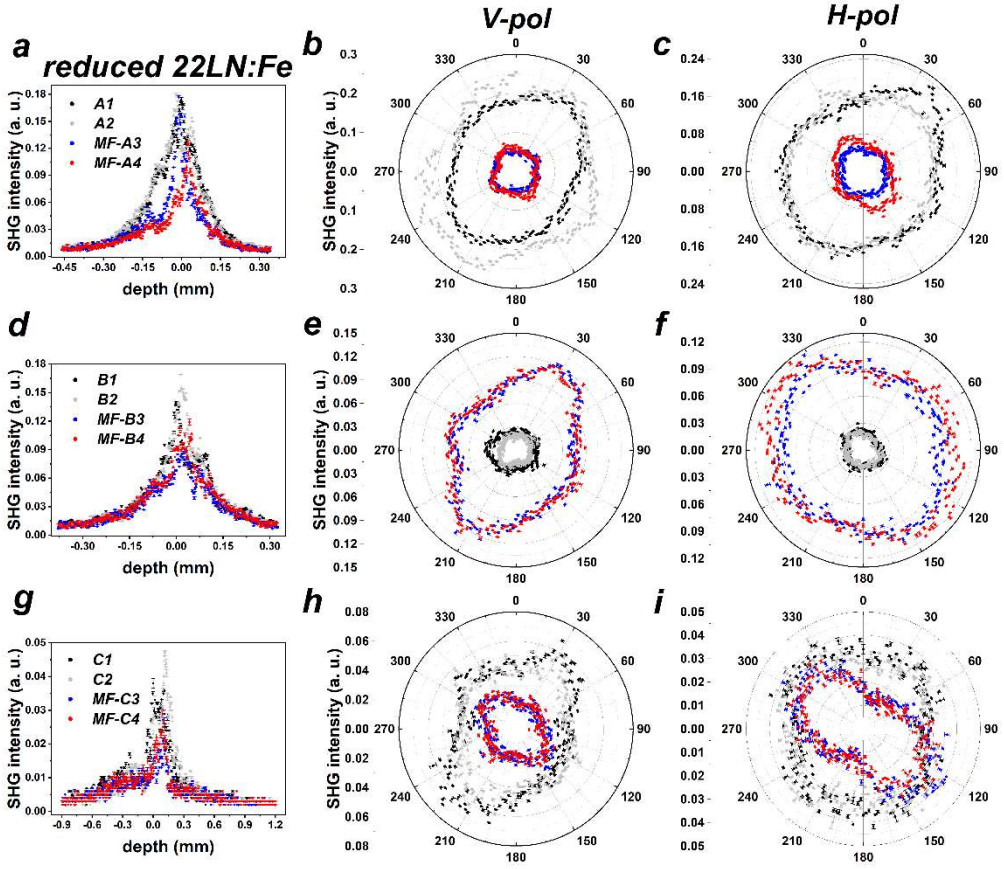

1006
1007 **Figure S9.** Reduced iron doped $LiNbO_3$ powders with doping concentration of 2.2 wt. % Fe_2O_3.

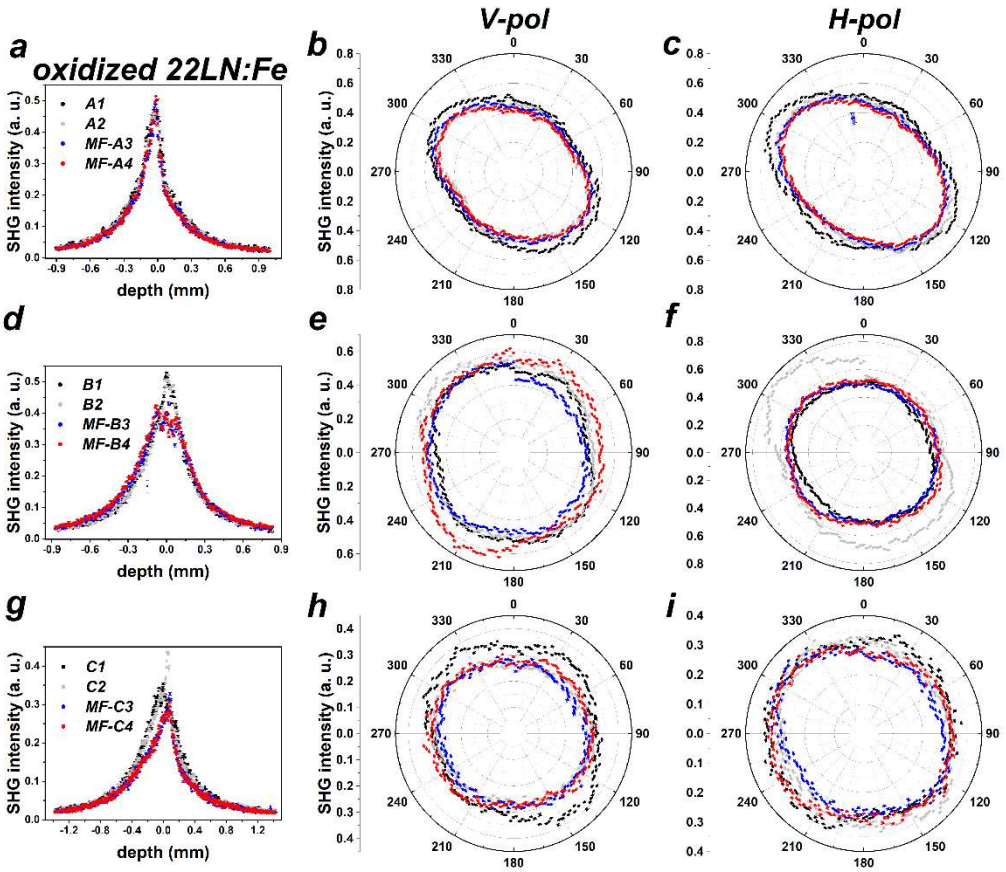

Figure S10. Oxidized iron doped $LiNbO_3$ powders with doping concentration of 2.2 wt. % Fe_2O_3.

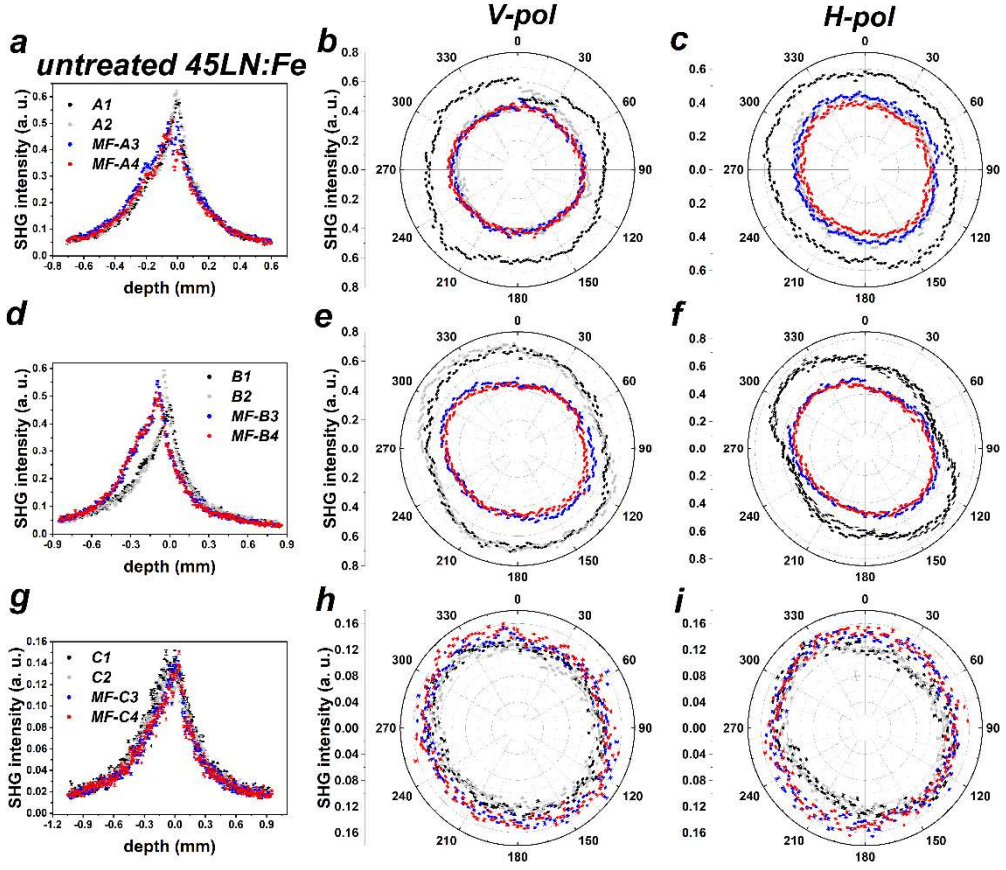

Figure S11. Iron doped $LiNbO_3$ powders with doping concentration of 4.5 wt. % Fe_2O_3.

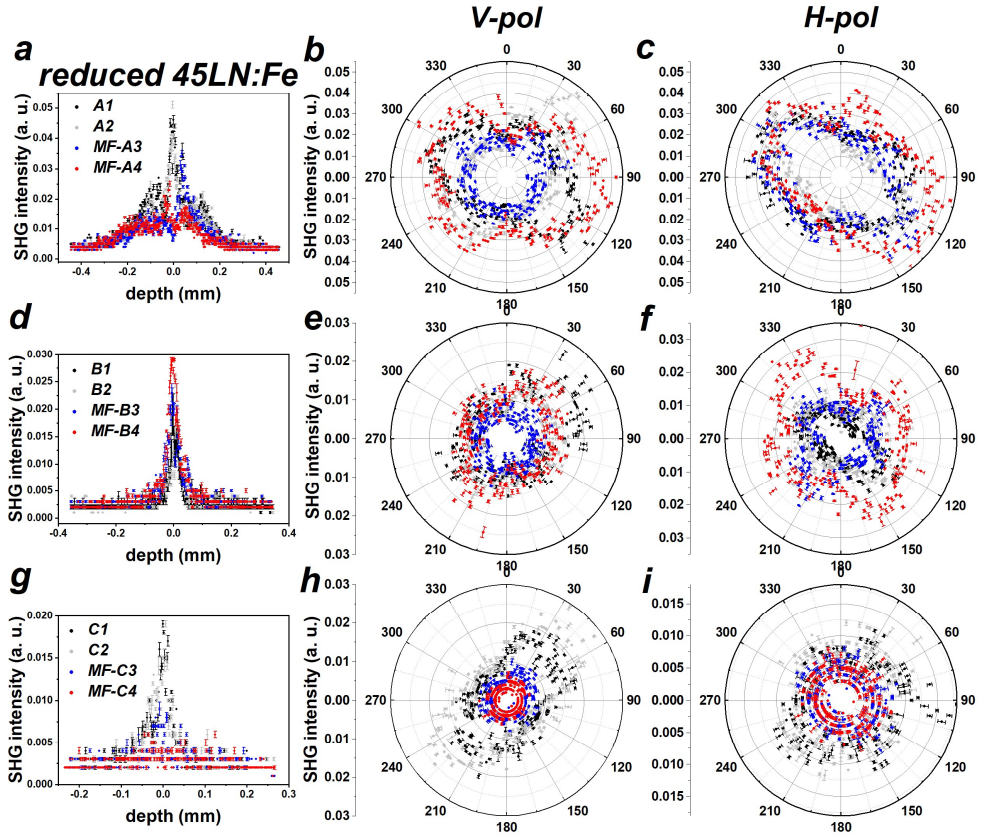

Figure S12. Reduced iron doped $LiNbO_3$ powders with doping concentration of 4.5 wt. % Fe_2O_3.

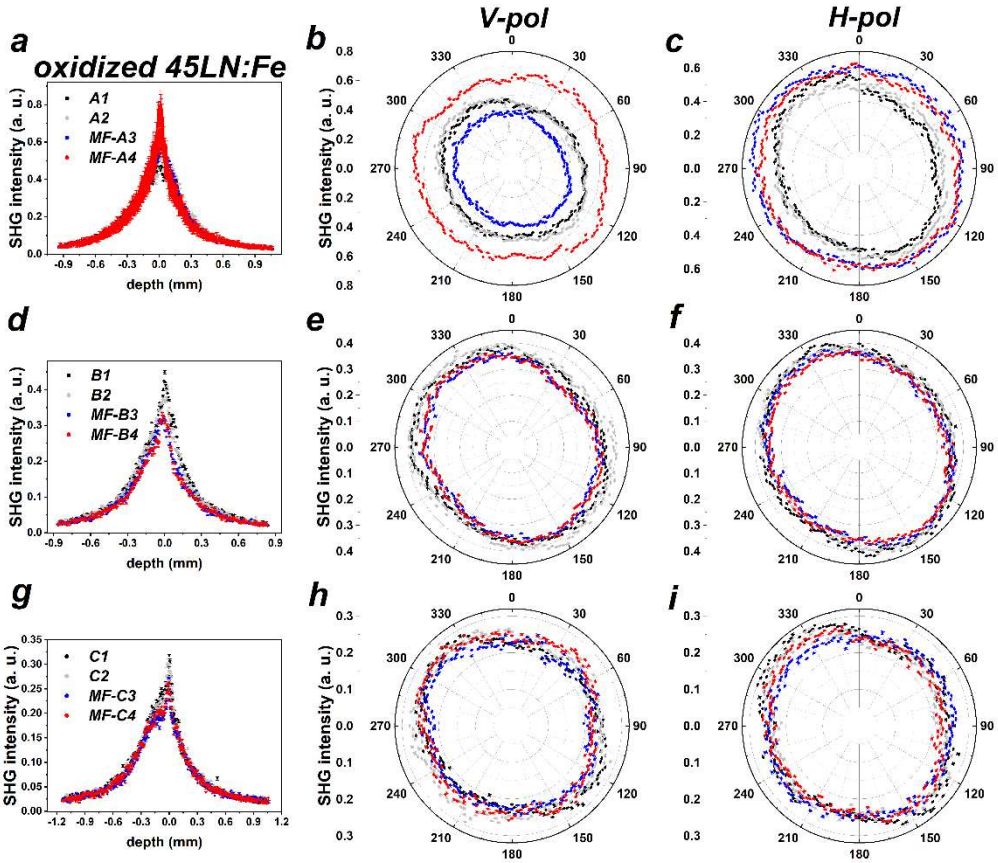

Figure S13. Oxidized iron doped $LiNbO_3$ powders with doping concentration of 4.5 wt. % Fe_2O_3.

References

[S1] R. D. Shannon, C. T. Prewitt, *Acta Cryst. B* **1969**, *25*, 925.

[S2] G. Pezzotti, *J. Appl. Phys.* **2013**, *113*, 211301.